Experimental determination of the propulsion matrix of the body of helical *Magnetospirillum magneticum* cells

Liu Yu (虞柳), Lucas Le Nagard, Solomon Barkley, Lauren Smith⬤, and Cécile Fradin⬤

Department of Physics and Astronomy, McMaster University, 1280 Main Street W, Hamilton, Ontario L8S4M1, Canada

Helical-shaped magnetotactic bacteria provide a rare opportunity to precisely measure both the translational and rotational friction coefficients of micron-sized chiral particles. The possibility to align these cells with a uniform magnetic field allows clearly separating diffusion along and perpendicular to their longitudinal axis. Meanwhile, their corkscrew shape allows detecting rotations around their longitudinal axis, after which orientation correlation analysis can be used to retrieve rotational diffusion coefficients in the two principal directions. Using light microscopy, we measured the four principal friction coefficients of deflagellated *Magnetospirillum magneticum* cells, and compared our results to that expected for cylinders of comparable size. We show that for rotational motions, the overall dimensions of the cell body are what matters most, while the exact body shape has a larger influence on translational motions. To obtain a full characterization of the friction matrix of these elongated chiral particles, we also quantified the coupling between the rotation around and translation along the longitudinal axis of the cell. Our results suggest that for this bacterial species cell body rotation could significantly contribute to cellular propulsion.

I. INTRODUCTION

The swimming of microorganisms takes place at low Reynolds number, where viscous forces play a dominant role [1–4]. As such, modeling the motion of these organisms requires a precise knowledge of their friction coefficients. In the case of flagellated bacteria, swimming involves opposite rotations of the cell body and flagella, resulting in an overall translation along the propulsion axis [5–7]. The tumbling motion used by many bacteria (notably *Escherichia coli*) to change direction and achieve chemotaxis involves a rotational diffusion of the propulsion axis [8,9]. Both translation along the propulsion axis and rotations are involved in the "U-turn" motion of magnetotactic bacteria (MTB) submitted to a magnetic field reversal [10,11]. These examples show the importance of determining all the friction coefficients of a particular microorganism (translational and rotational, along and perpendicular to the cell longitudinal axis) in order to fully understand its motility.

Although friction coefficients can in principle be calculated for bacteria with a cylindrical shape such as *E. coli*, things become more complicated for cells with more asymmetrical shapes. Here we are interested in the magnetotactic species *Magnetospirillum magneticum*, with the characteristic "corkscrew" shape representative of spirilla. The friction coefficients of spiral bacteria have been approximated by treating the cells as spheres [10], linear chains of spheres [12], cylinders [13,14], and prolate spheroids [15]. A more accurate model was recently obtained by taking the actual helical shape of the cells into account using finite element analysis [16]. An experimental approach, involving the construction of macroscopic models of spiral cells, was also used to estimate their friction coefficients [17]. None of these strategies, however,

accounts for the exact cellular shape, including irregularities and eventual appendages. In addition, none of the above studies delved into the coupling between rotation and translation expected for chiral objects.

Here we propose to experimentally measure the friction coefficients of deflagellated cells of the spirillum *M. magneticum* by recording their translational and rotational diffusion as observed with light microscopy. We take advantage of the asymmetric shape of spirilla, which allows a full determination of a cell's orientation from its projection in the focal plane [18,19]. We also take advantage of the magnetic properties of *M. magneticum*, which allows aligning the average direction of the longitudinal axis of the cells with that of an external magnetic field, and separately measuring transversal and longitudinal friction coefficients. We first show the results of simulations used to determine the best experimental strategy for extraction of the different friction coefficients of cells from their trajectories. We then present measurements of the friction coefficients as a function of cell length and compare them with different available theoretical models. Finally we experimentally quantify the coupling between rotation around and translation along the cell longitudinal axis.

II. METHODS

A. Simulations of rotational diffusion

Simulations of the rotational diffusion of a magnetotactic cell placed in a uniform magnetic field were performed using MATHEMATICA (Wolfram Research, code available online [20]). The cell was assimilated to an elongated rigid body with rotational symmetry around its longitudinal axis ($\vec{L}$), and rotational friction coefficients $f_{r_\perp}$ and $f_{r_\parallel}$, associated respectively with rotations perpendicular to and around $\vec{L}$.
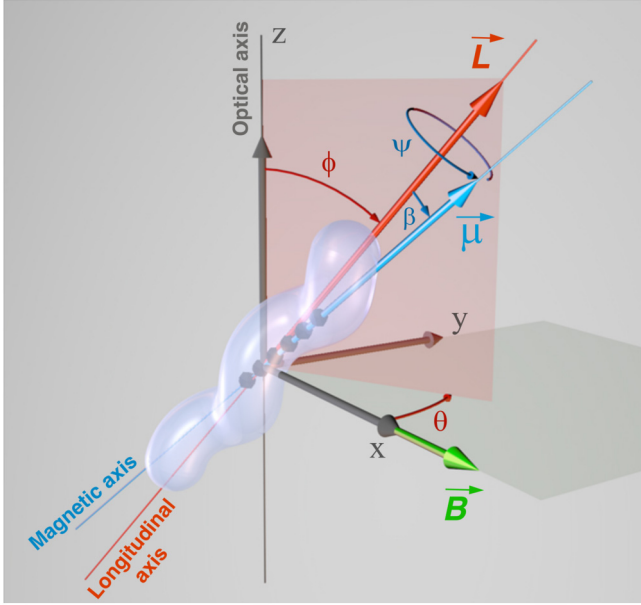
FIG. 1. Orientation of the cell with respect to the focal plane and external magnetic field ($\vec{B}$). The position of the cell longitudinal axis (defined by $\vec{L}$) is characterized by its inclination ϕ from the optical axis and by the angle θ between its projection in the focal plane and the magnetic field (aligned with $\vec{x}$). The direction of the cell magnetic moment ($\vec{\mu}$) is characterized by the angle β it makes with $\vec{L}$ and by the rotation ψ of the cell around its longitudinal axis.

The cell's magnetic moment, $\vec{\mu}$, was placed at a constant inclination (β) from $\vec{L}$, as illustrated in Fig. 1. The orientation of the cell was updated every $\delta t = 1$ ms, by performing a series of four small rotations. The cell was first allowed to diffuse around its three principal axes of rotation, $\vec{L}$, $\vec{L} \times \vec{z}$ and $\vec{L} \times (\vec{L} \times \vec{z})$, with an angular displacement drawn from a Gaussian distribution with variance $2D_r \delta t$, where $D_r = D_{r_\parallel} = kT/f_{r_\parallel}$ (axial rotational diffusion coefficient) for the rotation around $\vec{L}$, and $D_r = D_{r_\perp} = kT/f_{r_\perp}$ (transversal rotational diffusion coefficient) for the other two rotations. In the presence of an external magnetic field ($\vec{B}$), aligned with $\vec{x}$, an additional rotation was added to account for the magnetic torque. The cell as a whole (i.e., both $\vec{L}$ and $\vec{\mu}$) was rotated around $\vec{\mu} \times \vec{B}$, by an angle $|\vec{\mu} \times \vec{B}| \delta t/f_{r_\perp}$ (using $f_{r_\perp}$ as the friction coefficient, a very good approximation as long as β is small). At each step, the apparent orientation of the cell in the focal plane (θ) and around its longitudinal axis (ψ) were calculated from $\vec{L}$ and $\vec{\mu}$. θ was obtained by projecting $\vec{L}$ onto the $(\vec{x}, \vec{y})$ plane. ψ was calculated as the angle between the $(\vec{L}, \vec{z})$ plane (red plane in Fig. 1) and the vector $\vec{\mu} - (\vec{\mu} \cdot \vec{L}/L^2)\vec{L}$. Additional details about the simulations can be found in Appendix B. Simulations were typically run for 2000 steps (2 s) at $T = 300$ K, using physical parameters representative of those expected for *M. magneticum* cells: $D_{r_\perp} = 0.1$ s^{-1}, $D_{r_\parallel} = 0.01$–0.5 s^{-1}, and $\mu = 0.5 \times 10^{-15}$ A m^2 [19].

B. Cell culture

Cells of *M. magneticum* strain Aerobic species of Magnetotactic Bacterium (AMB-1) [21], obtained from ATCC (American Type Culture Collection, 700264), were grown according to the protocol detailed in Ref. [22]. Briefly, cells were grown at 30 °C in 60 mL of growth medium, containing trace mineral supplements, KH_2PO_4, $MgSO_4 \cdot 7H_2O$, HEPES, $NaNO_3$, yeast extract, soy bean peptone (BD Bacto Soytone), potassium lactate, and Fe(III) citrate (pH 7.0), inside 125-mL sealed glass bottles. Any O_2 in the headspace of the bottle and dissolved in the medium was removed by bubbling N_2 in the headspace and in the solution. The medium was then autoclaved to ensure sterility. Right before inoculation, 1 mL of O_2 was added to the headspace (65 mL) to reach a 1.5% O_2 mircoaerobic environment ideal for the growth of AMB-1 cells with strong magnetic properties. When needed in order to obtain data for longer cells, 10 µg/mL of cephalexin (Sigma-Aldrich), an antibiotic which can block cell division [23,24], was added to the growth medium two days after inoculation.

C. Cell imaging

Cells were harvested 3 to 5 days after inoculation, then killed and deflagellated by heating at 60 °C for 15 min. After cooling down to room temperature, the bacteria suspension was diluted 50-fold in fresh medium to achieve an ideal concentration for single cell observation (3 000–12 000 cells/µL). The diluted solution was then injected into a home-built sample chamber consisting of a glass slide and a microscope coverslip separated by two melted parafilm strips, creating a channel approximately 18 mm long, 5 mm wide, and 100–200 µm high. The chamber was sealed with vacuum grease or transparent nail polish to avoid evaporation and flow. Movies of cells undergoing translational and rotational diffusion were then immediately captured at 100 frames per second with a fast CCD camera (AVT Prosilica GE) mounted on a phase-contrast microscope (Nikon Eclipse E200-LED), with either a 40× (0.65 NA, pixel size 0.18 µm) or a 100× (1.25 NA, pixel size 0.07 µm) objective. The effective viscosity of the medium is larger than in the bulk when bacteria are close to a surface [25]. To avoid this issue, when studying cell diffusion we only imaged cells that were at least 20 µm away from the coverslip or glass slide. The stage of the microscope was modified with a pair of custom-made electromagnetic coils [19], so that constant uniform magnetic fields up to 1.7 mT could be applied parallel to the focal plane by circulating a current through the coils. The average movie duration was 17 s, with no movie shorter than 4 s. To determine cell body handedness, cells were immobilized in a hydrogel prepared from 17 mg/mL agar in deionized water [26]. The mixture was microwaved for several seconds until the agar was completely dissolved and injected into a warm sample chamber ($\approx$350 µm thick). The chamber was then immediately submerged into a fresh MTB culture, and a magnetic bar was used to impart a vertical orientation to the cells as the gel solidified.

D. Cell tracking

Cells were tracked using the algorithm illustrated in Fig. 2, and their shape and orientation determined assuming that the cells mostly laid in the focal plane, i.e., that $\phi \simeq \pi/2$ (a reasonable assumption since equipartition of energy leads to $\langle (\phi - \pi/2)^2 \rangle \simeq kT/(\mu B) < 0.1$ for $\mu = 0.5 \times 10^{-15}$ A m^2
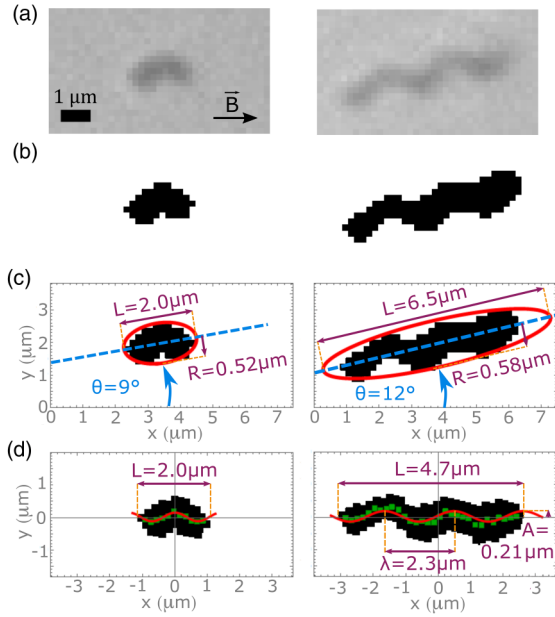
FIG. 2. Illustration of the image analysis process for a short cell (left panels) and a long cell (right panels) in a horizontal magnetic field $B = 0.1$ mT. (a) Phase microscopy images of the cells, (b) binarized images, (c) results of the ellipse fit, and (d) results of the sine fit after rotation of the cells to an horizontal position.

and $B > 0.1$ mT). Images of individual cells were first binarized using ImageJ [27], resulting in a connected cloud of points representing the cell in each frame of the movie [Fig. 2(b)]. The position of the cell was tracked by finding the center of mass of this cloud of points. The apparent orientation of the cell (θ) was determined in two different ways using a code written in MATHEMATICA (available online [28]). First, the cell was fit with an ellipse to obtain an estimate of the cell apparent orientation, θ, its length, L, and diameter, R [Fig. 2(c)]. While this method is fast and robust, it may not always capture the exact orientation of helical AMB-1 cells properly, and thus a more refined fit was then performed to take into account the sinusoidal shape of the cell body projected in the focal plane, as first described in Ref. [19] and as illustrated in Fig. 2(d). The approximate orientation of the cell, θ, was first quickly determined using a linear fit, and then the cell was rotated so as to lay approximately horizontal. Points were binned vertically to obtain a new series of points [green points in Fig. 2(d)] considered as the cell backbone, which was then fit with a sine function, $A \sin(2\pi x/\lambda + \psi)$, returning the amplitude (A) and wavelength (λ) of the cell helical backbone, as well as a phase (ψ) giving a direct representation of the rotation of the cell around its long axis (as long as the cell lays in the focal plane, or close to it, i.e., as long as $\phi \simeq \pi/2$). To further refine the determination of the cell apparent orientation (θ), the horizontal binarized cell image was rotated from $-8.5°$ to $+8.5°$ in $0.5°$ increments and the backbone determination and sine fit repeated at each step. The results of the fit with the least χ^2 were saved. To speed up the image analysis process, this full procedure was only performed for the first 100 frames. For the rest of the movie, the values of A and λ were fixed to the average values
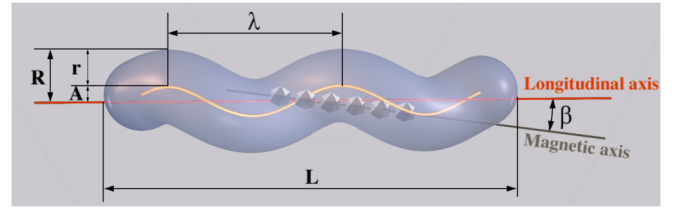

FIG. 3. Three-dimensional model of a *M. magneticum* cell. The helical backbone, longitudinal axis (which is also the propulsion axis), and magnetic axis (assumed to be exactly aligned with the magnetosome chain) are represented by a sinusoidal yellow line, a straight red line, and a straight slanted brown lines, respectively.

obtained from the first 100 fits, and only the parameters θ, ψ, and L were determined. The cell radius r (Fig. 3) was measured manually using ImageJ from images obtained at $100\times$ magnification. When comparing the results of the measurement of the apparent orientation of the cells in the focal plane (θ) with either the sine fit or the elliptical fit for the same images, we found that there was on average a $3.2°$ difference in the value of θ. The error on θ was estimated from the $\tau = 0$ interpolated intercept of the orientation correlation function, as explained in Appendix C 1, Fig. 13, and in Ref. [19]. It was found to be $\epsilon = 1.0°$ for the elliptical fit and $\epsilon = 2.5°$ for the sine fit ($B = 0.1$–0.2 mT). The error on ψ was estimated by the same method and found to be significantly larger, $\epsilon = 5.6°$ on average ($B = 1$ mT) (Appendix C 2 and Fig. 14). The cell lengths obtained using both methods were strongly correlated, with the length measured using the elliptical fit (length of the major axis) on average 28% larger than that measured with the sine fit (end-to-end distance). We used the median length obtained from the sine fits as the measurement of the cell length (such that the small fraction of measurements for which the cells were at a significant angle from the focal plane were not taken into account).

E. Orientation correlation functions

The orientation correlation function (OCF) relative to the apparent orientation of the cell in the focal plane, $\theta(t)$, is defined as

$$C_\perp(\tau) = \langle \cos[\theta(t+\tau) - \theta(t)]\rangle. \tag{1}$$

It can be calculated for each cell by averaging over all pairs of angles separated by a given lag time τ. If the cell is confined to the focal plane ($\phi = \pi/2$) and in the absence of a magnetic field, the exponential form $C_\perp(\tau) = e^{-D_{r_\perp}\tau}$ is expected, with a characteristic decay time inversely related to the transversal rotational diffusion coefficient $D_{r_\perp}$ [14,29]. The OCF relative to the orientation of the cell around its longitudinal axis, $\psi(t)$, is defined as

$$C_\parallel(\tau) = \langle \cos[\psi(t+\tau) - \psi(t)]\rangle. \tag{2}$$

In this case, it can be expected that $C_\parallel(\tau) = e^{-D_{r_\parallel}\tau}$.

In the presence of a magnetic field, $C_\perp(\tau)$ is not longer expected to decay to 0, as shown in Appendix D and discussed in Sec. III B 2. In addition, in the presence of experimental noise, the intercept of the OCF at $\tau = 0$ shifts from 1 to $1 - \sigma^2$ where σ^2 is the variance of the measurements of the

TABLE I. Physical parameters characterizing the geometry of the body of *M. magneticum* AMB-1 cells (L, cell length; λ, wavelength of the cell helical backbone; A, amplitude of the cell helical backbone; r, cell body radius; R, overall cell radius; β, angle between cell axis and cell magnetic moment). All reported values were experimentally measured in this study (L is the 1st to 99th percentile of the lengths obtained from an ellipsoidal fit of all the cells in two separate 30-s movies acquired at $20\times$ magnification, λ and A were obtained from the sine fits of $n = 63$ cells with L longer than the average λ, R from ellipsoidal fit of $n = 23$ cells with L longer than the average λ imaged at $100\times$ magnification, r from $n = 31$ cells imaged at $100\times$ magnification) except for β whose value was taken from Ref. [19]. Average values are reported as mean $\pm$ SD deviation, except for r where the error corresponds to the size of a single pixel in the image used to measure this parameter. Distributions for the values of these parameters can be found in Fig. 15.

L (μm)	λ (μm)	A (μm)	r (μm)	R (μm)	β (°)	Handedness
1.8–4.2 (no cephalexin)						
1.8–5.9 (with cephalexin)	2.5 ± 0.3	0.21 ± 0.03	0.26 ± 0.07	0.61 ± 0.06	6.5 ± 3.2	Left-handed

angle used to calculate the OCF (θ or ψ), as discussed in Appendix C.

III. RESULTS

A. *M. magneticum* structural parameters

1. Cell body dimensions

The structural parameters of *M. magneticum* AMB-1 cells (length L, wavelength λ, and amplitude A of the cell backbone, cell body radius r, and overall cell radius $R = A + r$, as illustrated in Fig. 3) were determined from phase microscopy images as explained in Sec. II D, and are summarized in Table I. The length of the cells varied from 1.8 to 4.2 μm in normal growth conditions, but increased noticeably upon addition of cephalexin (Table I, Appendix E, and Fig. 15). Other cell body characteristics did not vary noticeably across the population or with growth conditions (Fig. 15). Values of r and R might be slightly overestimated, the first because it is obtained by direct measurement of a thickness close to the diffraction limit, and the second because it comes from an elliptical fit of a helical structure. The cell helical backbone wavelength and amplitude, on the other hand, are obtained with great accuracy, despite the fact that the backbone amplitude is just below the resolution limit of the microscope ($A = 0.21$ μm on average for cells whose length is larger than the backbone wavelength and for which structural parameters can be determined reliably), because its value is obtained from the fit of the position of a cloud of points. This is demonstrated by the fact that the same value is obtained for A regardless of the image resolution: At $40\times$ magnification, we measured $\lambda = 2.54 \pm 0.23$ μm ($n = 40$) and $A = 0.20 \pm 0.04$ μm ($n = 40$), mean $\pm$ standard deviation (SD), while at $100\times$ magnification, we obtained $\lambda = 2.21 \pm 0.22$ μm and $A = 0.23 \pm 0.02$ μm ($n = 5$). These values are not affected by cephalexin (see Fig. 15): We measured $\lambda = 2.37 \pm 0.30$ μm and $A = 0.22 \pm 0.02$ μm for cephalexin-treated cells ($n = 18$, observed at $100\times$ magnification).

2. Cell body handedness

Species from the genus *Aquaspirillum* all have helical cell bodies, which can be right- or left-handed [30]. As there had been contradictory reports concerning the handedness of *M. magneticum* AMB-1 [31,32], we set out to determine the handedness of AMB-1 cells by taking z-stack images of immobilized cells. Imaging the body of 12 different cells attached to the microscope coverslip from top to bottom always revealed a pattern characteristic of a left-handed helix, as illustrated in Fig. 4(a). The same was true of two cells fixed in a gel and orientated perpendicular to the focal plane ($\phi = 0$) which, when the cross section of the cell body along the cell long
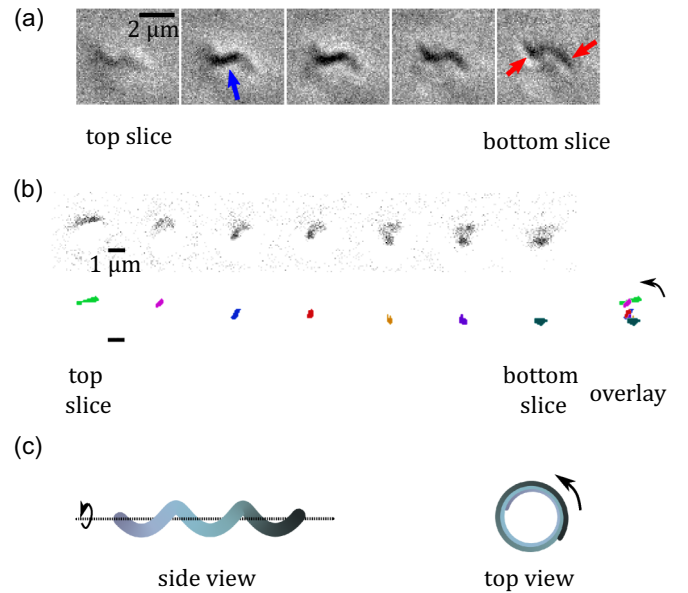

FIG. 4. (a): z-stack images (contrast adjusted) of a cell attached to a glass slide with the slices shown from top to bottom (vertical steps: 1 μm). Since the images were acquired in an upright microscope, the top slice shows the part of the cell closest to the observer. The blue arrow in panel 2 and red arrows in panel 5 indicate the middle and outer parts of the cell, respectively. (b) z-stack images of a vertical cell fixed in a gel (vertical steps: 0.8 μm), from the top slice (showing the part of the cell closest to the observer) to the bottom slice (showing the part of the cell furthest from the observer). The original (contrast-adjusted) images are shown in the top row, and binarized colorized versions of these images are shown below. On the right-hand side, an overlay of the colorized images demonstrates that the helical backbone of the cell follows a counterclockwise path when going from the nearest end to farthest end of the cell (curved black arrow), as expected for a left-handed helix. (c) Schematic side and top views of a left-handed helix.

axis was imaged, both displayed a counterclockwise pattern characteristic of left-handed helices [Figs. 4(b) and 4(c)].

The trajectories of flagellated bacteria swimming close to a solid surface also give indications about cell handedness. Hydrodynamic forces opposite in direction are exerted by the surface on a cell's rotating body and flagella, and this creates a torque on the cell resulting in a circular trajectory [25,33]. We observed that six cells close to a glass coverslip all had counterclockwise trajectories when observed from the water side of the water-glass interface (see the Supplemental Material [34]). This corresponds to the motion of cells whose flagellum is rotating clockwise (when looking from the back of the cell) and is therefore right-handed [33]. The rotation of the cell body must then be in the counterclockwise direction, presumably making it left handed. Thus all our observations point to a left-handed cell body.

It is intriguing that we measure a handedness that is different from that reported in Ref. [31]. However, we note that in that work handedness was inferred from images of horizontal cells taken in a single plane, which can give the impression that a cell has a different handedness depending on whether it lays slightly above or below the focal plane [see Fig. 4(a)].

B. Simulations of the rotational diffusion of an elongated magnetic particle

In order to determine the optimal experimental conditions to measure the diffusion coefficients of *M. magneticum* cells, we first performed simulations of the rotational diffusion of a cell (elongated rigid particle with longitudinal axis $\vec{L}$ and magnetic moment $\vec{\mu}$, separated by a fixed angle β) placed in an external magnetic field ($\vec{B}$), as described in Sec. II A.

1. Orientation distributions

We first considered the simple case where $\vec{\mu}$ is aligned with $\vec{L}$ ($\beta = 0$) and monitored the apparent orientation of the particle in the focal plane, $\theta(t)$, and around its longitudinal axis, $\psi(t)$. The case where $\beta > 0$ is discussed in Appendix F (Figs. 16–18). All simulations were started with the cell in the equilibrium position ($\phi = \pi/2$, $\theta = 0$). Examples of angular trajectories are shown in Fig. 5, illustrating the increased alignment of the particle with the magnetic field as B increases [Fig. 5(a)]. In contrast, the motion around the longitudinal axis is not affected by magnetic field strength [Fig. 5(b)]. The probability distribution for θ is expected to follow a Boltzmann distribution, which has a simple form if $\vec{L}$ is restricted to the focal plane (i.e., when $\phi = \pi/2$) [14]:

$$p(\theta) = e^{H\cos\theta}/[2\pi I_0(H)], \tag{3}$$

where I_n is the modified Bessel function of the first kind of order n, and $H = \mu B/kT$ represents the balance between magnetic and thermal forces. Fits of the simulated orientation distributions with Eq. (3) give an estimate of H, from which μ can be calculated [Figs. 5(c) and 5(d)].

Equation (3) is only strictly valid for particles constrained to rotations in the focal plane. Thus as B increases and the particles pass from a free 3D to a quasi-2D motion (with $\phi \simeq \pi/2$), we expect the values of μ obtained by fitting
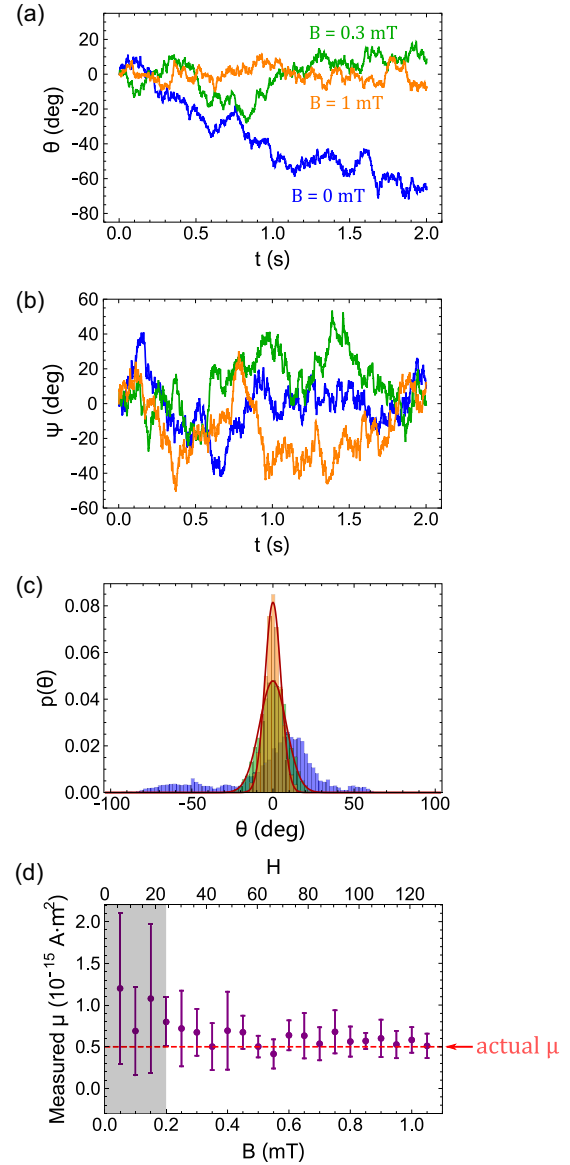

FIG. 5. Angular trajectories obtained from simulations of elongated magnetic particles ($\beta = 0$). [(a), (b)] Examples of angular trajectories for $\theta(t)$ and $\psi(t)$ at different magnetic field strengths. (c) Orientation distributions for θ obtained as a result of 20 s simulations, with a fit to a simple Boltzmann distribution [Eq. (3)]. Same color scheme as in panels (a) and (b). (d) Values of the magnetic moment obtained from the fit of θ distributions (mean ± SD for $n = 10$ simulations each equivalent to a 2-s experiment).

particle orientation distributions with Eq. (3) to become more accurate. Indeed, our simulations show that for $B \geqslant 0.2$ mT, the correct value of μ is recovered [Fig. 5(d)].

2. Orientation correlation functions

We used our simulations to explore in which conditions the rotational diffusion coefficients of the particle could be recovered from OCF. In principle, the rotational diffusion coefficient of elongated particles perpendicular to their long axis, $D_{r\perp}$, can be extracted from $C_\perp(\tau)$, the OCF related to the particle's apparent orientation in the focal plane $\theta(t)$ [35].

When only thermal fluctuations influence the rotational diffusion and when the diffusion is restricted to the focal plane ($\phi = \pi/2$), the OCF takes an exponential form, with a characteristic decay time equal to the rotational diffusion persistence time $\tau_P = 1/D_{r_\perp}$. However, in the presence of a magnetic field, the orientation of a magnetic particle such as a MTB will become correlated at long time, and the OCF will tend toward $[I_1(H)/I_0(H)]^2$ (see Appendix D). We have thus previously proposed the following phenomenological expression for the OCF [14]:

$$C_\perp(\tau) = \left[1 - \left(\frac{I_1(H)}{I_0(H)}\right)^2\right]e^{-\tau/\tau_P'} + \left(\frac{I_1(H)}{I_0(H)}\right)^2. \quad (4)$$

At short lag time, thermal motions are expected to dominate and the OCF should decay at the rate of $dC_\perp/d\tau = -D_{r_\perp}$ regardless of the value of H, which implies that $\tau_P' = \{1 - [I_1(H)/I_0(H)]^2\}/D_{r_\perp}$ (see Appendix D for details). The simulated OCF are indeed fitted well with Eq. (4) [Fig. 6(a)], and the fit returns both μ and $D_{r_\perp}$, calculated from the values of H and τ_P' extracted from the fit, respectively [Figs. 6(b) and 6(c)]. The values obtained at very small fields are not accurate, both because the relaxation times are then larger than the measurement times, and because Eq. (4) was written assuming a 2D trajectory. However, as soon as $H \geqslant 5$ (i.e., $B \geqslant 0.05$ mT for a typical *M. magneticum* AMB-1 cell with $\mu \simeq 0.5 \times 10^{-15}$ A m^2) an accurate measurement of $D_{r_\perp}$ is obtained [Fig. 6(c), black symbols]. We also verified that $D_{r_\perp}$ could be estimated by simply fitting OCF with a linear function (with slope $-D_{r_\perp}$) over a short time range (Taylor expansion of $C_\perp(\tau)$ at small τ), which is useful when dealing with OCF calculated from short and noisy angular trajectories. We found that $D_{r_\perp}$ could indeed be determined this way as long as the linear fit is done for $\tau < 50$ ms [Fig. 6(c), empty symbols].

The same analysis was done for the rotational diffusion of the particle around its long axis, using two different values of $D_{r_\parallel}$. This rotation is not affected by the presence of a magnetic field, and thus $C_\parallel(\tau)$ is expected to exponentially decay to zero with an initial rate $-1/D_{r_\parallel}$, independently of B. This is what we observed when simulating particles with $D_{r_\parallel} = 0.5$ s^{-1} [Fig. 7(a)], allowing an accurate measurement of $D_{r_\parallel}$ at all fields from the fit of the OCF [Fig. 7(b)]. However, when using a lower $D_{r_\parallel} = 0.01$ s^{-1} value in the simulations, we observed that the slope of $C_\parallel(\tau)$ changed with B and that the measurements of $D_{r_\parallel}$ obtained from the fit of the $C_\parallel(\tau)$ were inaccurate at low B [Fig. 7(b)]. This is because the OCF is calculated from values of ψ estimated as the angle between the vertical plane containing the long axis of the particle (red plane in Fig. 1) and a vector perpendicular to $\vec{L}$. This is done in order to exactly reproduce what happens in experiments, where ψ is experimentally accessible only from the analysis of the shape of the projection of the cell body in the focal plane. The estimated ψ is a good approximation of the real ψ only when $\vec{L}$ is close to being aligned with the focal plane ($\phi \simeq \pi/2$). We conclude that it is safer to use $H > 60$ (i.e., for particles with a magnetic moment similar to that of a typical AMB-1 cell, $B > 0.5$ mT) in order to accurately measure $D_{r_\parallel}$ from the fit of the OCF.
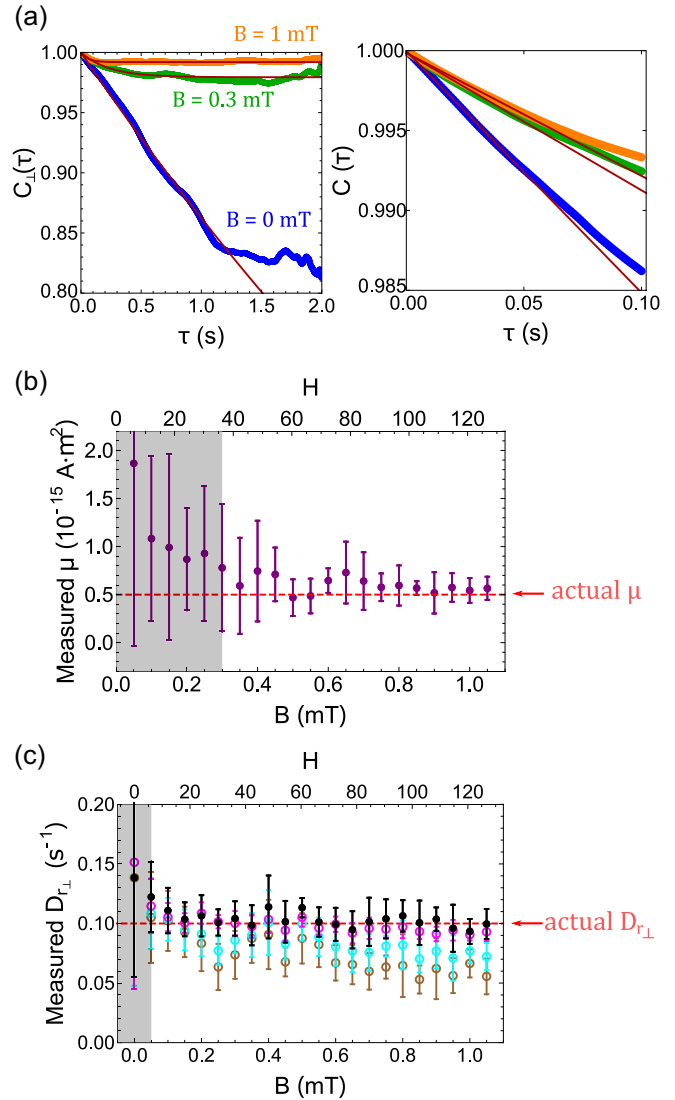

FIG. 6. Simulation results for the rotation perpendicular to the particle longitudinal axis. (a) Left panel: OCF for $\theta(t)$, $C_\perp(\tau)$, at different magnetic field strengths, fit with Eq. (4) for the first 1 s. Right panel: Close up on the first 100 ms of the OCF with linear fit for the first 50 ms. (b) Values of the magnetic moment μ obtained from fitting the OCF with Eq. (4) for the first 1 s. (c) Value of the rotational diffusion coefficient $D_{r_\perp}$ obtained from the fit of $C_\perp(\tau)$. Magenta (very dark gray), cyan (light gray), and brown (dark gray) empty symbols are for linear fits on the first 10, 50, and 100 ms of the OCF, respectively. Filled black symbols are the result of a fit on the first 100 ms of the OCF with Eq. (4). In panels (b) and (c), all data points show the mean ± SD for $n = 10$ simulations, each equivalent to a 2-s experiment.

C. Experimental observation of *M. magneticum* diffusion

1. Rotation perpendicular to the cell longitudinal axis

To study the rotational diffusion of cells around an axis perpendicular to their longitudinal axis, we recorded the motion of *M. magneticum* AMB-1 cells rendered nonmotile by a short heat treatment. This treatment both kills and deflagellates the cells [36]. Cells were then placed in uniform magnetic fields with $B = 0.1$ to 0.2 mT, as our simulations suggested that at these low field strengths the cells were already constrained to
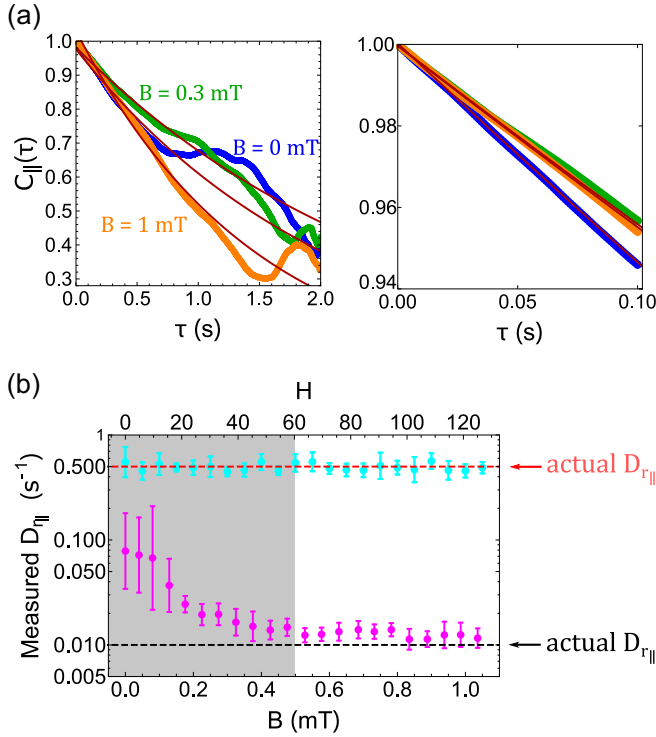
FIG. 7. Simulation results for the rotation around the particle longitudinal axis. (a) Left panel: $C_\parallel(\tau)$, the OCF for the estimated $\psi(t)$, at different fields, with exponential fits to the first 1 s of data. Right panel: Closeup on the first 100 ms of the OCFs with exponential fits to the first 50 ms of data. (b) Values of the rotational diffusion coefficient $D_{r_\parallel}$ obtained from fitting $C_\parallel(\tau)$. Here, magenta (dark gray) and cyan (light gray) empty symbols are for exponential fits to the first 50 ms of the OCFs (mean $\pm$ SD for $n = 10$ simulations each equivalent to a 2-s experiment) for two different values of $D_{r_\parallel}$.

the focal plane ($\phi \simeq \pi/2$), allowing accurate measurements of $D_{r_\perp}$ [Fig. 6(c)]. Using field values as low as possible ensured that the cells still displayed a significant distribution of orientations in the focal plane, making the measurements of changes in orientation, and therefore calculation of the OCFs, more precise. The orientation of the cells in the focal plane (θ) and body length (L) were obtained by fitting the image of the cells in each available movie frame, as explained in Sec. II D and Fig. 2. In normal growth conditions, most cells have a length between $L = 1.8$ and 4.2 μm (as observed in previous studies [14,19]). To explore a broader range of cell lengths, we also used cells grown in the presence of 10 μg/mL cephalexin, which increased this range up to 5.9 μm.

Orientation distributions and OCF were generated for each cell [Figs. 8(a) and 8(b)]. The orientation distributions were usually not centered around $\theta = 0$ [Fig. 8(a)], a sign that only the relaxation associated with rotational diffusion was observed during the finite observation time (about 10 s), and not the relaxation associated with the rotation of the cell body around the average direction of the magnetic moment (expected for cells with a misalignment between $\vec{L}$ and $\vec{\mu}$, as discussed in Appendix F). The position of the peak, which does not depend on cell length, is random depending on the initial position of the cell at the beginning of the experiment. Thus, a simple linear analysis of the OCF at short lag times
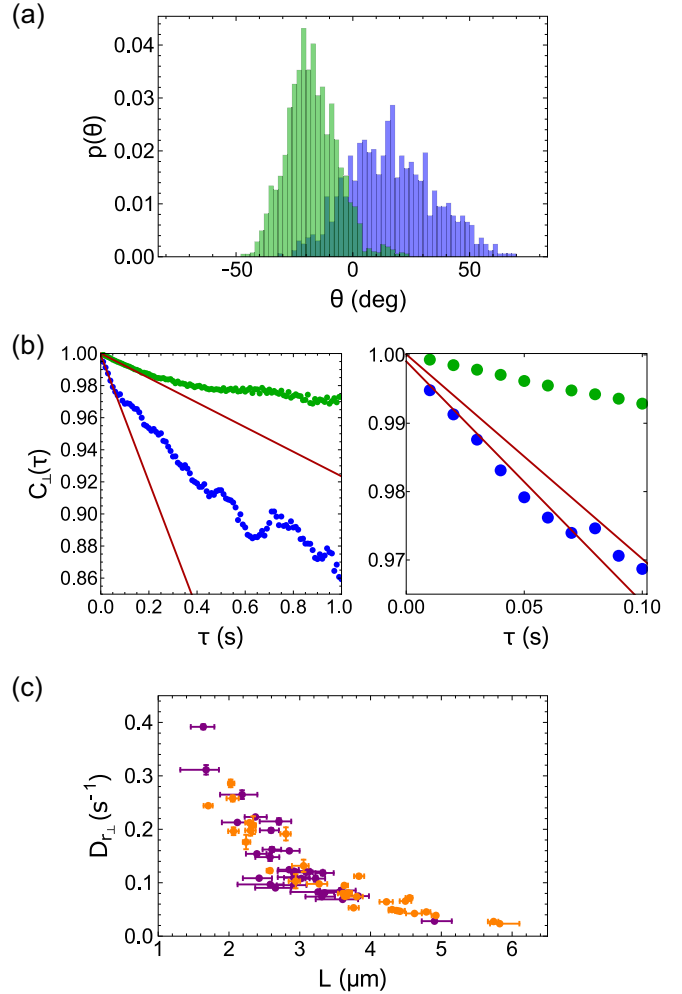

FIG. 8. Experimental observation of the rotational diffusion of cells perpendicular to their longitudinal axis. (a) Examples of orientation distributions (angle θ) recorded for a short cell [$L = 1.6$ μm, blue (dark gray) bars] and a long cell [$L = 3.8$ μm, green (light gray) bars] over 8.38 s ($B = 0.1$ mT), and (b) corresponding OCF [same color scheme as in panel (a), lines are linear fits based on the first 0.05 s of the OCF]. The right panel is a close up on the short time range of the OCF. (c) Measured rotational diffusion coefficient $D_{r_\perp}$ as a function of cell length [purple (dark gray) symbols: data obtained at 40× magnification with $B = 0.1$ mT; orange (light gray) symbols: data obtained at 100× magnification with $B = 0.2$ mT, and including cephalexin-treated cells]. The error on L was estimated using the first and third quartiles of the lengths measured for that cell over the entire movie. The error on $D_{r_\perp}$ is the SD of values obtained from the fit of the OCF over different time ranges from 0 to 50 ms.

τ was performed for each cell [Fig. 8(b)] in order to obtain the value of its rotational diffusion coefficient $D_{r_\perp}$. As expected for elongated particles, $D_{r_\perp}$ sharply and monotonously decreases as cell length increases [Fig. 8(c)].

2. Rotation around the cell longitudinal axis

To study the rotation of the cells around their longitudinal axis, the experimental protocol was modified in two ways. First, we used a higher magnetic field ($B = 1$ mT), since our simulations suggested that $D_{r_\parallel}$ could be correctly estimated
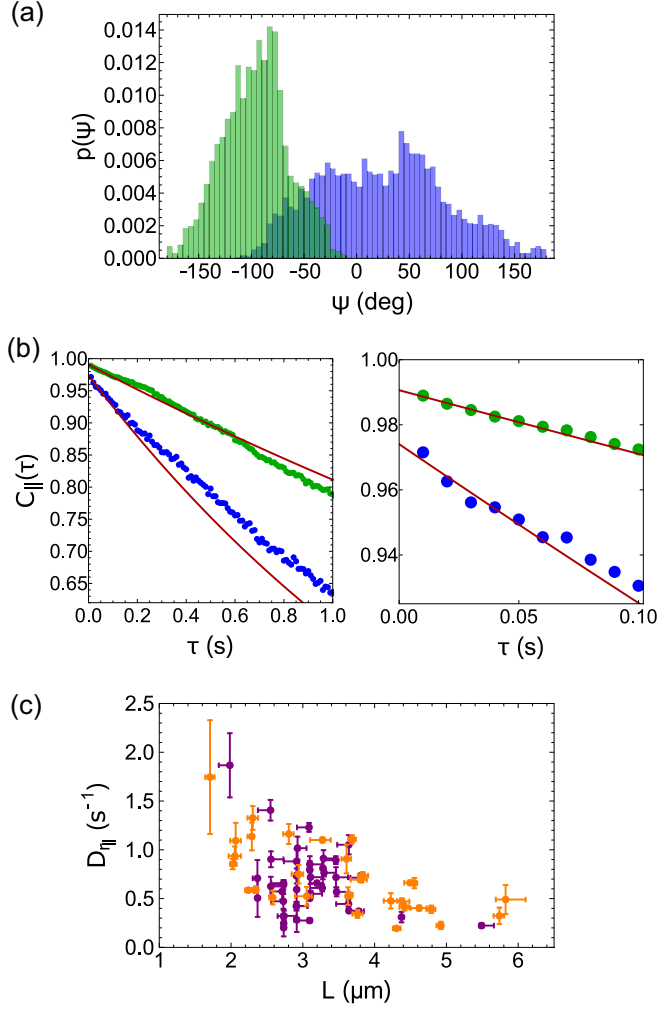
(a)

(b)

(c)

FIG. 9. Experimental observation of the rotational diffusion of cells around their longitudinal axis. (a) Examples of orientation distributions (angle ψ) obtained for a short [$L = 2.4$ μm, blue (dark gray) bars] and a long cell [$L = 5.5$ μm, green (light gray) bars] over 21 s at $B = 1$ mT. (b) Corresponding OCF [same color scheme as in panel (a), right panel is a closeup of the first 0.1 s of the OCF]. Lines are exponential fits of the OCF for the first 0.05 s. (c) Measured rotational diffusion coefficient $D_{r_\parallel}$ as a function of cell length. Purple (dark gray) and orange (light gray) symbols represent data obtained at $40\times$ and $100\times$ magnification, respectively. Error bars were calculated as in Fig. 8(c).

from the fit of the OCF only for $B > 0.5$ mT. Second, for each image, the shape of the projection of the cell backbone in the focal plane was determined and fitted to a sine function to estimate both the cell orientation in the focal plane, θ, and the angular position around its longitudinal axis, ψ (see Sec. II D for details). The relationship between θ and ψ allowed us to obtain, for each cell, the misalignment angle β between magnetic moment and longitudinal axis (see Appendix F and Fig. 16 for details) as done in Ref. [19]. Examples of orientation distributions and OCF associated with ψ are shown in Figs. 9(a) and 9(b). From the intercept of these OCF at $\tau = 0$, it is clear that the error made on ψ, measured for $B = 1$ mT [Fig. 9(b)] is much larger than the one made on θ, measured for $B = 0.1$ or 0.2 mT [Fig. 8(b)]. However, this
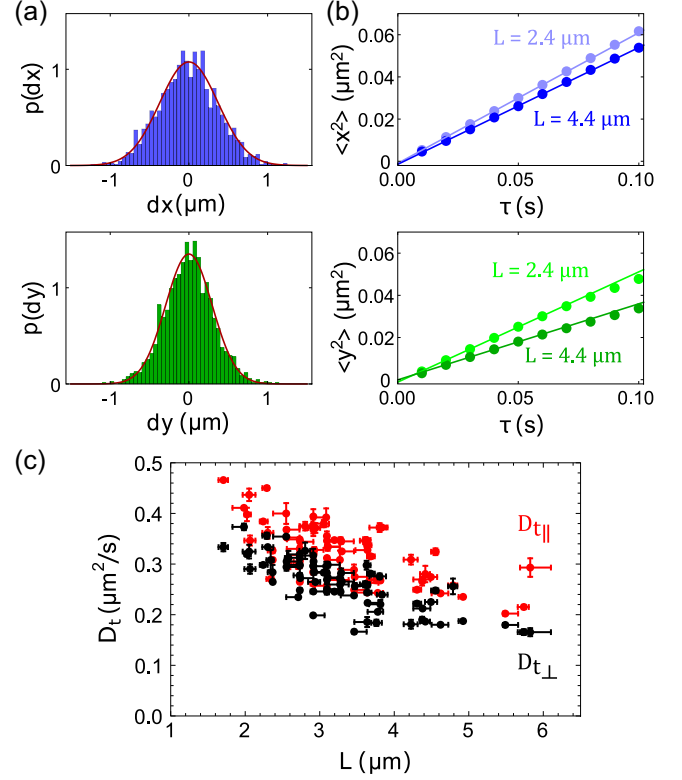

(a)

(b)

(c)

FIG. 10. Experimental observation of the cells translational diffusion. (a) Examples of distributions of displacements after a time interval $\tau = 10$ ms along (upper panel, blue bars) and perpendicular (lower panel, green bars) to the cell longitudinal axis, here for a cell with length $L = 4.4$ μm at $B = 1$ mT. (b) MSD and linear fit for $\tau = 0$ to 0.05 s for a short cell (light colors, $L = 2.4$ μm) and a long cell (dark colors, $L = 4.4$ μm). (c) Translational diffusion coefficients along ($D_{t_\parallel}$, black symbols) and perpendicular [$D_{t_\perp}$, red (light gray) symbols] to the cell long axis. Error bars were calculated as in Fig. 8(c).

error decreases as L increases (see Fig. 14). Exponential fit of the OCF associated with ψ returned an estimate for the rotational diffusion coefficient $D_{r_\parallel}$ for each cell. Cells with a misalignment angle $\beta \geqslant 10°$ were omitted from the results altogether, since accurate estimates of $D_{r_\parallel}$ then become difficult (see Fig. 18). Despite the scattering in the data, it is clear that $D_{r_\parallel}$ decreases when the cell length increases, and that in general $D_{r_\parallel}$ is higher than $D_{r_\perp}$, as expected for an elongated particle [Fig. 9(c)].

3. Translational diffusion

Data obtained at high magnetic field give the opportunity to estimate the two principal translational friction coefficients of the cells, since constraining their direction along that of the external magnetic field allows easily separating diffusion along and perpendicular to the cell longitudinal axis. Distributions of displacements along (x direction) and perpendicular to (y direction) the cell longitudinal axis are Gaussian [Fig. 10(a)], as expected for a simple diffusion process. The mean-squared displacement (MSD) as a function of lag time was calculated for each cell in both directions [examples are shown in Fig. 10(b)]. Linear fits of these MSD at short lag times returned the corresponding translational diffusion coef-
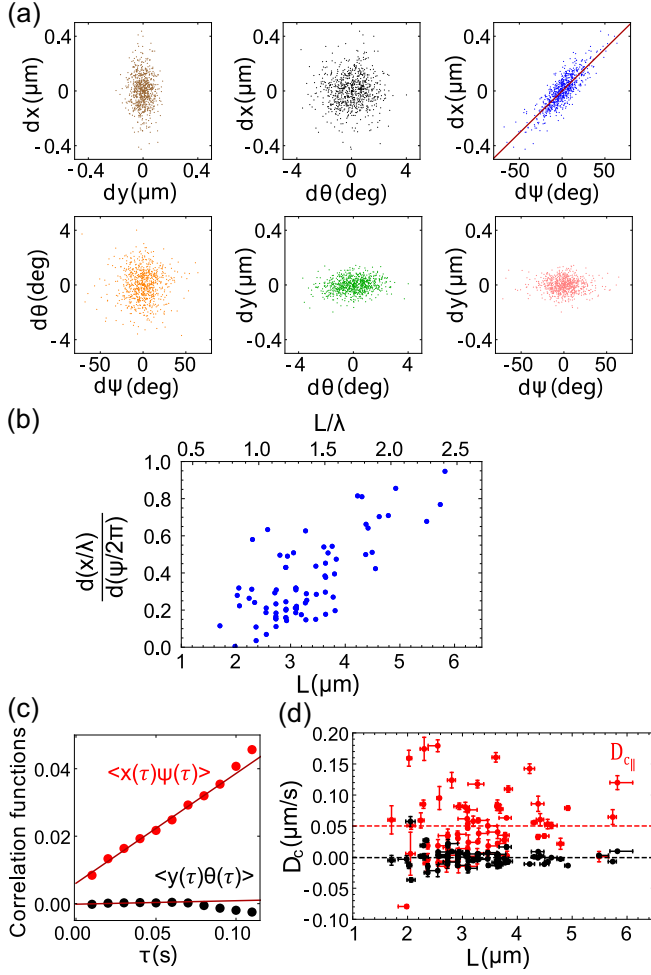
FIG. 11. Experimental observation of the coupling between rotation around and translation along the cell longitudinal axis. (a) Example of the relationship observed between different types of displacements (dx, dy) and rotations $(d\theta, d\psi)$ for one particular cell. Each point represents the cell's displacement during a $\Delta t = 0.01$ s time interval (i.e., between two consecutive frames). The line in the dx vs $d\psi$ plot is a linear fit of the data. (b) $dx/d\psi$ in units of $\lambda/2\pi$ for all studied cells. (c) Correlation functions $\langle x(\tau)\psi(\tau)\rangle$ and $\langle y(\tau)\theta(\tau)\rangle$ calculated for a particular cell, with linear fit for $\tau = 0$ to 0.05 s. (d) Coupling diffusion coefficient parallel to the cell long axis $D_{c_\parallel} = \langle x(\tau)\psi(\tau)\rangle/(2t)$ [red (light gray) symbols, 0.05 μm/s average] compared to $\langle y(\tau)\theta(\tau)\rangle/(2t)$ (black symbols, 0 μm/s average). Error bars were calculated as in Fig. 8(c).

ficients. Both $D_{t_\parallel}$ and $D_{t_\perp}$ clearly decrease with cell length [Fig. 10(c)], with the diffusion coefficient perpendicular to the cell longitudinal axis ($D_{t_\perp}$) on average smaller than the diffusion coefficient parallel to that axis ($D_{t_\parallel}$).

4. Coupling between rotation and translation

For chiral objects such as helices, a coupling between the rotation around and translation along the helical axis is expected. We indeed detected such a coupling for individual cells, as evidenced by a correlation between the displacement along the cell longitudinal axis (dx) and rotation around that axis ($d\psi$) when observed between two consecutive frames [Fig. 11(a)]. In contrast, no such correlation was observed

for any other pairs of displacements (dx, dy) and rotations $(d\theta, d\psi)$. The coupling between dx and $d\psi$ was quantified in two ways. First, we considered the average value of $dx/d\psi$ for each cell, which we found increased linearly with cell length and approached the maximal value of $\lambda/2\pi$ for long cells [Fig. 11(b)]. Second, we looked at the correlation function $\langle x(\tau)\psi(\tau)\rangle$, which should be equal to $2D_{c_\parallel}\tau$ (see Appendix A). We indeed observe that $\langle x(\tau)\psi(\tau)\rangle$ is linear at short lag times [Fig. 11(c)], although the correlation is often lost at larger τ. Using only the very short-term part of the correlation function, we measured the coupling diffusion coefficient along the cell long axis to be $D_{c_\parallel} \simeq 0.05$ μm/s on average, in very clear contrast to what is observed perpendicular to the cell long axis [Fig. 11(d)].

IV. DISCUSSION

The detection of the position and orientation of nonmotile *M. magneticum* AMB-1 cells allowed us to separately measure the five diffusion coefficients necessary to fully characterize their Brownian motion. From these five diffusion coefficients, the five friction coefficients found in their propulsion matrix can be calculated, fully defining the drag forces experienced by the elongated chiral cell body. For rotations and translations perpendicular to the cell longitudinal axis, for which there is no coupling, the friction coefficients (f) are simply related to the corresponding diffusion coefficients by $f_{i\perp} = kT/D_{i\perp}$, where $i = t$ or r. In the axial direction, however, a clear coupling between rotation and translation is detected (Fig. 11). Although it remains relatively weak ($D_{c_\parallel}^2/(D_{t_\parallel}D_{r_\parallel}) \lesssim 7\%$ according to our measurements), it needs to be taken into account when calculating the axial translational and rotational friction coefficients [Eqs. (A14) and (A15) in Appendix A]. The last friction coefficient, the axial coupling friction coefficient, is given by $f_{c_\parallel} = kTD_{c_\parallel}/(D_{t_\parallel}D_{r_\parallel} - D_{c_\parallel}^2)$ [Eq. (A16)]. The five friction coefficients of the body of AMB-1 cells, taking into account the correction due to coupling in the axial direction, are plotted as a function of cell body length in Fig. 12.

The friction coefficients of bacteria are often estimated by assimilating the cell body to a particle with simple geometry, usually a sphere or a cylinder. The translational and rotational friction coefficients of cylinders, which have been calculated with great precisions for a range of aspect ratios (see Appendix A), can serve as a useful comparison to those of the helical *M. magneticum* cells. For each friction coefficient, we binned the data by cell length, and fit the resulting curves with the expression expected for a cylinder (see Fig. 19). We found that both the rotational and the translational coefficients of the cells were very close to those expected for a cylinder. For rotations, cells behave as cylinders of radius $\rho \simeq 0.43$ to 0.51 μm, just below the overall radius of the cell, $R = 0.61$ μm. For translations, on the other hand, they behave as cylinders of radius $\rho \simeq 0.37$ to 0.40 μm, a value closer to the radius of the cell body, $r = 0.26$ μm. Thus, for rotations the overall dimensions of the cell body seems to be what matters most, whereas for translations the exact radius of the body is also important. In all cases, the friction coefficients of *M. magneticum* cells are on average larger than that of a cylinder with a radius equal to that of the cell body, a
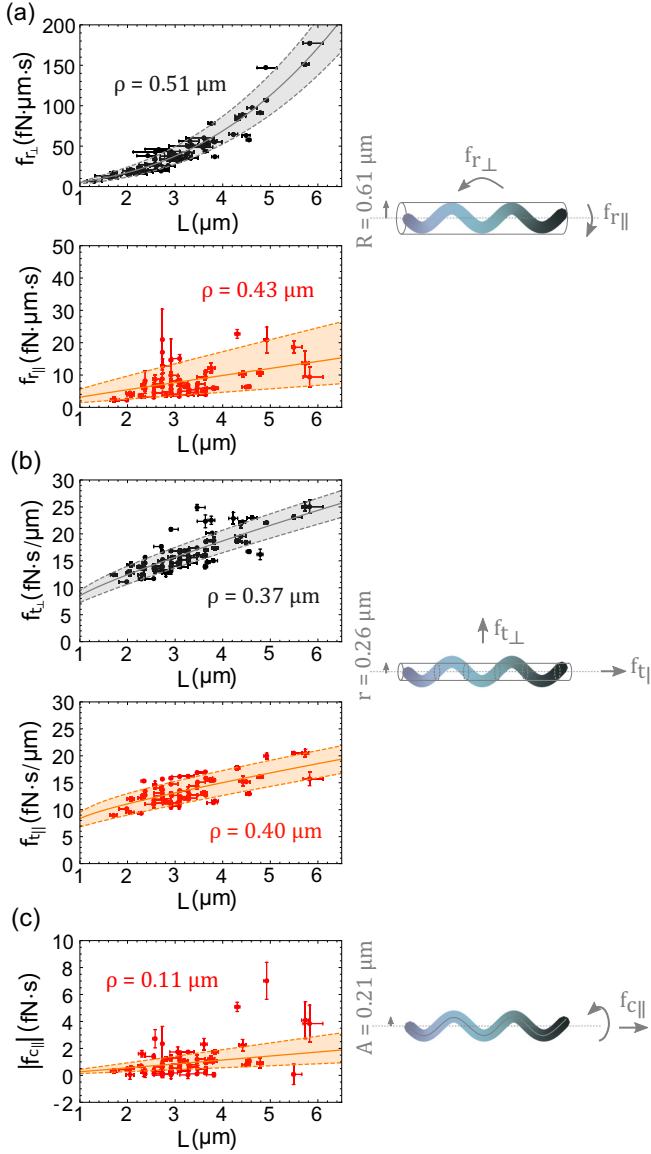
FIG. 12. Dependence of AMB-1 friction coefficients on cell length. (a) Rotational friction coefficients, $f_{r\perp}$ (upper panel, black symbols) and $f_{r\parallel}$ (lower panel, red symbols). The solid lines show a fit of the binned data with the expressions expected for a cylinder of radius ρ [Eqs. (A7) and (A8)], giving $\rho = 0.51$ μm ($f_{r\perp}$) and $\rho = 0.43$ μm ($f_{r\parallel}$), very close to the overall cell radius R (as illustrated in the right panel). The shaded areas represent the range of values expected for up to 30% variations of ρ. (b) Translational friction coefficients, $f_{t\perp}$ (upper panel, black symbols) and $f_{t\parallel}$ (lower panel, red symbols). The solid lines are fit of the binned data with the expressions expected for a cylinder of radius ρ [Eqs. (A4) and (A5)], giving $\rho = 0.37$ μm ($f_{t\perp}$) and $\rho = 0.40$ μm ($f_{t\parallel}$). These values are intermediate between R and the cell body radius, r. The shaded areas represent the range of values expected for up to 30% variations of ρ. (c) Axial coupling friction coefficient. The solid line is a fit of the binned data with the expressions expected for a helix of radius ρ [Eq. (A11)], yielding $\rho = 0.11$ μm, very close to the value of the cell backbone amplitude, A, as illustrated on the right. The shaded areas the values expected for up to 30% variations of ρ.

result in agreement with theoretical estimates (using Stokesian dynamics and the boundary integral method) of some of the friction coefficients of another spirillum, *Magnetospirillum gryphiswaldense* MSR-1 [16]. But in contrast to what was reported for MSR-1, we did not observe any variation of the cell overall radius with cell length and accordingly we see that on average AMB-1 friction coefficients vary with cell length exactly as expected for a cylinder of constant radius. There is, however, a lot of dispersion in the data, which cannot entirely be explained by experimental errors. Instead, invoking a 30% variation in ρ accounts for this dispersion (Fig. 12), which suggests that cells with the same length might have slightly different radius or morphology, maybe due to the presence of different appendages, for example, because of incomplete deflagellation. For *E. coli*, the presence of flagella increases translational friction coefficients by about 30%, and the rotational friction coefficient $f_{r\perp}$ by about 70% [37,38]. Although *M. magneticum* cells are amphitrichous (with only two flagella, one at each end of the cell), while *E. coli* cells are peritrichous (with a number of flagella distributed over the cell body), we can expect a roughly similar increase for AMB-1 friction coefficients in the presence of flagella.

For the nonzero axial coupling friction coefficient of AMB-1 cells, a better theoretical model for comparison with the data is that of a thin helical filament, for which $f_{c\parallel}$ can be estimated [Eq. (A11) in Appendix A]. We therefore fitted the experimentally obtained values of $f_{c\parallel}$ with Eq. (A11), and since this equation involves the values of $f_{t\parallel}$ and $f_{r\parallel}$, we fixed these values to the experimentally measured values of these coefficients, as approximated by their fit in Figs. 12(a) and 12(b). Despite the dispersion in the data, the trend observed is in agreement with the slow increase with cell length expected for a helical filament of radius $\rho = 0.11$ μm $\pm$ 30% [Figs. 12(c) and 19], close to the value of the cell backbone amplitude. The large dispersion in the data in this case is due to the relatively large error made on the detection of the axial rotation (Fig. 9).

For translational motions, we find that $f_{t\perp} > f_{t\parallel}$ [Fig. 12(b)], as expected for elongated particles, but far from $f_{t\perp} = 2f_{t\parallel}$, the expected limit for long and thin filaments [39]. Indeed, the aspect ratio for the *M. magneticum* cells studied here was limited to the range $p = 1.5$ to 6. Their dimensions are similar to that of other small spirilla such as *S. gracile*; however, many other spirilla are longer, with larger aspect ratios [40]. The thin filament approximation might thus be appropriate for other spirilla. For rotational motions, we also have $f_{r\perp} > f_{r\parallel}$, and this is especially pronounced at large L [Fig. 12(a)]. Thus, the cell body is optimized for rotations around its long axis (as happens during flagellar swimming), but not for rotations perpendicular to the cell's long axis (as may happen during changes in cell orientation). For the natural range of AMB-1 cell lengths (2 to 4 μm), the characteristic timescale for changes in direction of the cell axis due to rotational diffusion is $\tau_{r\perp} = 1/D_{r\perp} = 3$ to 30 s. This is too slow for rapid changes in swimming direction, and indeed AMB-1 cells do not make use of rotational diffusion when they need to change direction. Instead, since they are amphitrichous, they reverse their propulsion direction by

changing the direction of rotation their flagella [31]. Other bacteria, such as *E. coli*, solve this problem in a different way, by using active rotational diffusion during tumbles in order to speed up changes in direction [29].

The measurement of the axial friction coefficients allows to calculate the drag force $\mathcal{F}_{\mathrm{drag}}^{\mathrm{body}}$ and torque $\mathcal{L}_{\mathrm{drag}}^{\mathrm{body}}$ applied to the AMB-1 cell body when swimming (average swimming speed $V \simeq 20$ μm/s and average angular velocity $\Omega \simeq 200$ rad/s). Since $f_{t_{\parallel}} = 13 \pm 2$ fN s/μm and $f_{r_{\parallel}} = 7 \pm 4$ fN μm s (mean $\pm$ SD for 2.5–3.5 μm long cells) we find that $\mathcal{F}_{\mathrm{drag}}^{\mathrm{body}} = f_{t_{\parallel}} V \simeq 0.26 \pm 0.04$ pN and $\mathcal{L}_{\mathrm{drag}}^{\mathrm{body}} = f_{r_{\parallel}} \Omega \simeq 1 \pm 1$ pN·μm. The drag force on the cell body is likely much larger than that on the flagella, so the overall drag force on the cell is $\mathcal{F}_{\mathrm{drag}}^{\mathrm{cell}} \simeq \mathcal{F}_{\mathrm{drag}}^{\mathrm{body}}$. Because swimming takes place as low Reynold's number, $\mathcal{F}_{\mathrm{drag}}^{\mathrm{cell}}$ is also equal to the total propulsive force (thrust) of the cell, which is thus on the order of $\simeq 0.26 \pm 0.04$ pN. This value is comparable to the thrust estimated for *E. coli* and *Salmonella typhimurium* [41,42], but significantly larger than that previously estimated for AMB-1 [43].

Further considering that $|f_{c_{\parallel}}| \simeq 0.7 \pm 0.7$ fN· s allows us to calculate the propulsive thrust due to the rotation of the cell body alone: $\mathcal{F}_{\mathrm{thrust}}^{\mathrm{body}} = |f_{c_{\parallel}}| \Omega \simeq 0.1 \pm 0.1$ pN. It is interesting that the propulsive thrust is comparable to the drag force $\mathcal{F}_{\mathrm{drag}}^{\mathrm{body}}$ experienced by the cell body, because it suggests that the chiral shape of the body of AMB-1 cells is an important contribution to the cell propulsion, significantly adding to the propulsion contributed by the flagella. A different conclusion was reached for *Helicobacter pylori*, from hydrodynamic calculations based on body and flagella shape and dimensions [18]. However, the cell body diameter of *M. magneticum* is thinner than that of *H. pylori*.

Friction coefficients had never, to our knowledge, been measured directly for any type of bacterial cell before this study. Our results illustrate the fact that slight differences in dimensions can results in large differences in friction coefficients, especially rotational friction coefficients. This highlights the importance of single cell characterization for precise studies of bacterial swimming motions, or for studies where friction needs to be precisely estimated in order to measure propulsion and magnetic or optical torques using torque balance (e.g., measurements of the torque generated by the flagellar motor [44–46] or measurement of the magnetic moment of a cell with the U-turn method [10]).

The MATHEMATICA notebook used to perform these simulations is available online [20].

APPENDIX A: FRICTION COEFFICIENTS OF AN ELONGATED PARTICLE

1. Propulsion matrix

The drag forces on a rigid body are characterized by the friction coefficient tensor (also known as resistance matrix or propulsion matrix):

$$\mathcal{K} = \begin{pmatrix} A & B \\ B^T & D \end{pmatrix}. \tag{A1}$$

At low Reynold's numbers, this tensor can be used to express the external force and torque, $\vec{\mathcal{F}}$ and $\vec{\mathcal{L}}$, applied to the object, as a function of its velocity and angular velocity, $\vec{V}$ and $\vec{\Omega}$:

$$\begin{pmatrix} \vec{\mathcal{F}} \\ \vec{\mathcal{L}} \end{pmatrix} = \mathcal{K} \begin{pmatrix} \vec{V} \\ \vec{\Omega} \end{pmatrix}. \tag{A2}$$

2. Translation matrix for a short cylinder

For a particle with revolution symmetry, and the x axis aligned with the symmetry axis, the translation submatrix is diagonal:

$$A = \begin{pmatrix} f_{t_{\parallel}} & 0 & 0 \\ 0 & f_{t_{\perp}} & 0 \\ 0 & 0 & f_{t_{\perp}} \end{pmatrix}, \tag{A3}$$

where $f_{t_{\parallel}}$ and $f_{t_{\perp}}$ are the translational drag coefficients parallel and perpendicular to the object long axis.

For a sphere of diameter L, $f_{t_{\parallel}} = f_{t_{\perp}} = 3\pi\eta L$ (where η is the solvent viscosity). But for an elongated particle (length L, radius ρ), $f_{t_{\parallel}} < f_{t_{\perp}}$, and both coefficients vary with the aspect ratio of the particle, $p = L/(2\rho)$. For cylinders with $2 < p < 30$, these coefficients were calculated with great precision by modeling the particle surface with a series of beads and found to be well approximated by [47–49]

$$f_{t_{\parallel}} \simeq \frac{2\pi\eta L}{\ln p - 0.207 + 0.980/p - 0.133/p^2} \tag{A4}$$

and

$$f_{t_{\perp}} \simeq \frac{4\pi\eta L}{\ln p + 0.839 + 0.185/p + 0.233/p^2}. \tag{A5}$$

An expression for the translational drag coefficient of a thin helix along its axis has also been derived, but without taking into account the effect of the ends of the particle, in which case $f_{t_{\parallel}} \propto L$ [50].

3. Rotation matrix for a short cylinder

The rotation submatrix of a particle with revolution symmetry is also diagonal:

$$D = \begin{pmatrix} f_{r_{\parallel}} & 0 & 0 \\ 0 & f_{r_{\perp}} & 0 \\ 0 & 0 & f_{r_{\perp}} \end{pmatrix}. \tag{A6}$$

For a sphere, $f_{r_{\parallel}} = f_{r_{\perp}} = \pi\eta L^3$. For cylinders with $2 < p < 30$ a good approximation is [48,51]

$$f_{r_{\parallel}} \simeq \pi\eta L R^2 \times 3.84[1 + 0.677/p - 0.183/p^2] \tag{A7}$$

for axial rotations and

$$f_{r_{\perp}} \simeq \frac{\pi\eta L^3}{3[\ln p - 0.662 + 0.917/p - 0.050/p^2]} \tag{A8}$$

for rotations about the cylinder short axes. An expression for the rotational drag coefficient of a thin helix around its axis has also been derived, but without taking into account the effect of the ends of the particle, in which case $f_{r_{\parallel}} \propto L$ [50].

4. Coupling matrix for a thin helix

The coupling matrix is $B = 0$ for a particle with true revolution symmetry, meaning that rotations are decoupled from translational motions [52,53]. However, for a chiral particle such as a helix, there is a coupling between axial translation and rotation, and therefore

$$B = \begin{pmatrix} f_{c_\parallel} & 0 & 0 \\ 0 & 0 & 0 \\ 0 & 0 & 0 \end{pmatrix}, \tag{A9}$$

where $f_{c_\parallel} > 0$ for a right-handed helix and $f_{c_\parallel} < 0$ for a left-handed helix.

For a thin left-handed helix with length L, radius ρ, pitch λ, and and thickness r [50],

$$f_{c_\parallel} = -\frac{4\pi^2 \rho^2 \lambda}{\left[\log_{10}(r/(2\lambda)) + \frac{1}{2}\right](4\pi^2 \rho^2 + \lambda^2)} \eta L. \tag{A10}$$

When $\rho \ll \lambda$, one can show that [33]:

$$f_{c_\parallel} \simeq -(f_{r_\parallel} - \rho^2 f_{t_\parallel})\frac{2\pi}{\lambda}. \tag{A11}$$

For a more general analysis of the correlation between rotational and translational diffusion in the case of a particle of arbitrary shape, see Ref. [54].

5. Relationship between friction coefficients and diffusion coefficients

For a particle undergoing Brownian motion, writing the Langevin equations and applying the equipartition theorem leads to the diffusion tensor $\mathcal{D} = kT \, \mathcal{K}^{-1}$, and to the following expressions for the mean-squared displacements and rotations of the object [55]:

$$\langle x^2(t) \rangle = 2D_{t_\parallel} t = 2\frac{kT f_{r_\parallel}}{f_{t_\parallel} f_{r_\parallel} - f_{c_\parallel}^2} t,$$

$$\langle y^2(t) \rangle = \langle z^2(t) \rangle = 2D_{t_\perp} t = 2\frac{kT}{f_{t_\perp}} t,$$

$$\langle \omega_x^2(t) \rangle = 2D_{r_\parallel} t = 2\frac{kT f_{t_\parallel}}{f_{t_\parallel} f_{r_\parallel} - f_{c_\parallel}^2} t,$$

$$\langle \omega_y^2(t) \rangle = \langle \omega_z^2(t) \rangle = 2D_{r_\perp} t = 2\frac{kT}{f_{r_\perp}} t, \tag{A12}$$

as well as the following correlations:

$$\langle x(t)\omega_x(t) \rangle = -2D_{c_\parallel} t = -2\frac{kT f_{c_\parallel}}{f_{t_\parallel} f_{r_\parallel} - f_{c_\parallel}^2} t,$$

$$\langle x(t)y(t) \rangle = \langle \omega_x(t)\omega_y(t) \rangle = 0,$$

$$\langle x(t)\omega_y(t) \rangle = \langle \omega_x(t)y(t) \rangle = 0. \tag{A13}$$

Thus, the particle friction coefficients are related to its diffusion coefficients by

$$f_{t_\parallel} = kT\frac{D_{r_\parallel}}{D_{t_\parallel}D_{r_\parallel} - D_{c_\parallel}^2}, \quad f_{t_\perp} = kT\frac{1}{D_{t_\perp}}, \tag{A14}$$

$$f_{r_\parallel} = kT\frac{D_{t_\parallel}}{D_{t_\parallel}D_{r_\parallel} - D_{c_\parallel}^2}, \quad f_{r_\perp} = kT\frac{1}{D_{r_\perp}}, \tag{A15}$$

and

$$f_{c_\parallel} = kT\frac{D_{c_\parallel}}{D_{t_\parallel}D_{r_\parallel} - D_{c_\parallel}^2}. \tag{A16}$$

APPENDIX B: SIMULATIONS OF THE ROTATIONAL DIFFUSION OF A CELL IN THE PRESENCE OF A MAGNETIC FIELD

To simulate the rotational diffusion of a magnetotactic bacterial cell, we assimilated the cell to a small elongated particle with rotational symmetry (characterized by the two drag coefficients $f_{r_\parallel}$ and $f_{r_\perp}$) and a magnetic moment ($\vec{\mu}$) found at an angle β from the particle long axis. The orientation of this particle was characterized by two unit vectors, $\vec{u}_L$ representing the orientation of the cell long axis (with polar coordinates θ and ϕ, as defined in Fig. 1), and $\vec{u}_\mu$ representing the orientation of the cell magnetic moment (initially defined by the angles θ and $\phi + \beta$).

To simulate the rotational diffusion of this particle we performed, at each step δt in the simulation, three small rotations around the three principal axis of rotations, defined by the vectors $\vec{u}_\phi = \vec{u}_L \times \vec{z}$, $\vec{u}_\alpha = \vec{u}_L \times (\vec{u}_L \times \vec{z})$ and $\vec{u}_\psi = \vec{u}_L$. The magnitude of these rotations were randomly drawn at each step from the distributions:

$$p(\delta\phi) = \frac{e^{-d\phi^2/(4D_{r_\perp}\delta t)}}{\sqrt{4\pi D_{r_\perp}\delta t}}, \tag{B1}$$

$$p(\delta\alpha) = \frac{e^{-d\alpha^2/(4D_{r_\perp}\delta t)}}{\sqrt{4\pi D_{r_\perp}\delta t}}, \tag{B2}$$

$$p(\delta\psi) = \frac{e^{-d\psi^2/(4D_{r_\parallel}\delta t)}}{\sqrt{4\pi D_{r_\parallel}\delta t}}, \tag{B3}$$

where the rotational diffusion coefficients are calculated from the corresponding drag coefficients $D_{r_\perp} = kT/f_{r_\perp}$ and $D_{r_\parallel} = kT/f_{r_\parallel}$.

The influence of the magnetic field was taken into account by adding a fourth rotation around the vector $\vec{u}_\mu \times \vec{x}$ (since the magnetic field was chosen to be aligned with $\vec{x}$), by an angle $|\vec{\mu} \times \vec{B}|\delta t/f_{r_\parallel}$.

At the end of each step, after these four rotations were performed, the orientation of the cell in the focal plane [the (x, y) plane], which is equal to the azimuthal angle θ of $\vec{u}_L$ in polar coordinates, was recorded. The apparent orientation of the cell around its longitudinal axis, ψ, was calculated as follows:

$$\sin\psi = \cos((\vec{z} \times \vec{u}_L) \cdot \vec{v})/|\vec{z} \times \vec{u}_L|, \tag{B4}$$

where $\vec{v}$ is a unit vector in the plane defined by $\vec{L}$ and $\vec{\mu}$, perpendicular to $\vec{L}$ and pointing toward the same half-plane as $\vec{\mu}$ [20].

APPENDIX C: ERROR ON CELL ORIENTATION MEASUREMENT

1. Effect of measurement error on the OCF

If the error $\delta\theta$ on the measurement of θ is normally distributed with variance σ^2, then the OCF calculated from such
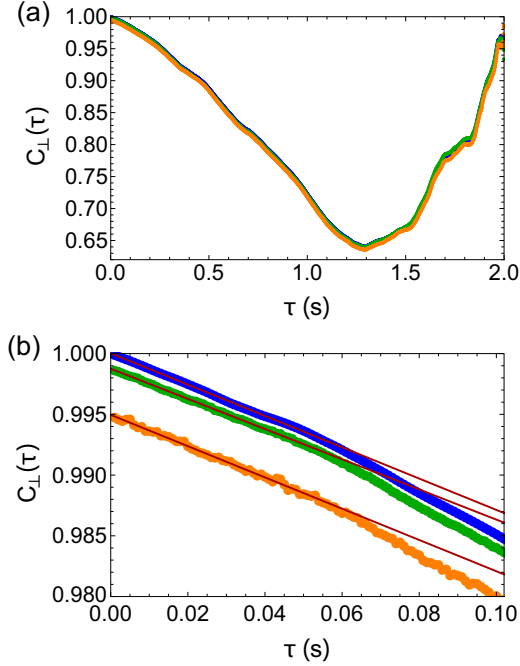
(a)

(b)

FIG. 13. Influence of measurement noise on the OCF. (a) Three OCFs are shown, calculated from the same trajectory ($B = 0$), with either no noise added [blue (very dark gray) curve] or noise added at each step on the measurement of the value of θ. The noise was drawn from a normal distribution with a full width at half maximum of $5°$ [corresponding to a variance $\sigma^2 = 0.00137$ rad^2, green (dark gray) curve] or $10°$ [corresponding to a variance $\sigma^2 = 0.00549$ rad^2, orange (light gray) curve]. (b) Closeup of the first 100 ms of the OCF shown in panel (a), with a linear fit of the first 50 ms of the data.

measurements becomes

$$C_\perp^N(\tau) = C_\perp(\tau)\langle\cos^2\delta\theta\rangle \simeq C_\perp(\tau)(1 - \sigma^2). \quad \text{(C1)}$$

The whole OCF is multiplied by a factor $(1 - \sigma^2)$. As a consequence, instead of having an intercept of 1 at $\tau = 0$, it has an intercept of $1 - \sigma^2$. This is indeed what is observed when measurement noise is added in the simulations: At very short lag times, when the OCF approaches 1, measurement errors result in a downward shift of the OCF by exactly σ^2 (Fig. 13). Thus, such an offset should also be expected in experimental OCF, and the variance of the experimental error can be recovered by considering the vertical intercept of experimental OCF.

2. Experimental error on the measurement of cell orientation

Using the intercept of the experimental OCF (as explained in Appendix C 1) allowed retrieving the standard deviation of the measurement error (σ) for each cell, for both angles θ and ψ (Fig. 14). The error made on θ is very small (on the order of $1°$). It is significantly larger for ψ (on the order of $5°$). As the cell length increases, the error on both angles monotonously decreases.
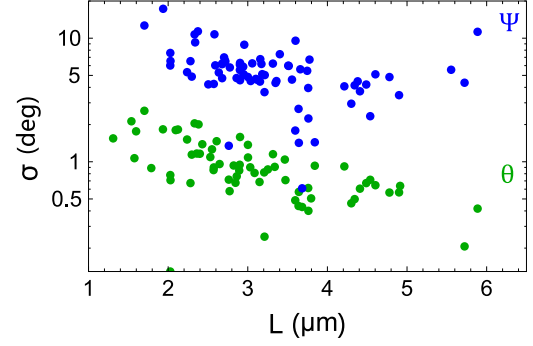

FIG. 14. Standard deviation (σ) of the error on the value of the angle θ measured using an elliptical fit [green (light gray)] and on the value of ψ measured using a sine fit [blue (dark gray)], plotted as a function of cell length. In both cases, σ was obtained for each individual cell from the intercept of the OCF computed from the angle measurements for that cell.

APPENDIX D: ORIENTATION CORRELATION FUNCTION IN THE PRESENCE OF A MAGNETIC FIELD

The orientation correlation function (OCF) related to the apparent focal plane orientation of a cell is given by

$$C_\perp(\tau) = \langle\cos[\theta(t + \tau) - \theta(t)]\rangle$$
$$= \langle\cos\theta(t)\cos\theta(t + \tau)\rangle + \langle\sin\theta(t)\sin\theta(t + \tau)\rangle, \quad \text{(D1)}$$

where brackets indicate average over time. Below we discuss the short-time and long-time asymptotic behavior of the OCF, and based on this we propose an expression for the OCF in the presence of a magnetic field.

1. Long-time behavior

At long time ($\tau \to \infty$), the values of $\theta(t)$ and $\theta(t + \tau)$ become uncorrelated and

$$C_\perp(\tau) = \langle\cos\theta(t)\rangle\langle\cos\theta(t + \tau)\rangle + \langle\sin\theta(t)\rangle\langle\sin\theta(t + \tau)\rangle. \quad \text{(D2)}$$

In the particular case of a magnetic field directed along the x axis, by symmetry $\langle\sin\theta(t)\rangle = 0$, resulting in

$$C_\perp(\infty) = \langle\cos\theta(t)\rangle^2. \quad \text{(D3)}$$

The value of $C_\perp(\infty)$ is determined by the distribution of orientations of the cell at equilibrium, $p(\theta)$:

$$C_\perp(\infty) = \left[\int_{-\pi}^{\pi} p(\theta)\cos\theta \, d\theta\right]^2. \quad \text{(D4)}$$

When the ratio $H = \mu B/(kT)$ is high ($H > 10$, a condition always realized in our experiments), the axis of the cells can be considered almost parallel to the focal plane, and the distribution of orientations is given by Eq. (3) leading to

$$C_\perp(\infty) = [I_1(H)/I_0(H)]^2. \quad \text{(D5)}$$

(Note that because of a typo, this equation was incorrectly written down in Ref. [14]). For a very strong magnetic field ($H \to \infty$), we get as expected $C_\perp(\infty) = 1$.

2. Short-time behavior

To characterize the short-time behavior of the OCF, we express it in terms of the characteristic function of the random variable $\Delta\theta(\tau) = \theta(t + \tau) - \theta(t)$:

$$C_\perp(\tau) = \text{Re}\langle e^{i\Delta\theta(\tau)}\rangle. \tag{D6}$$

Assuming $\Delta\theta(\tau)$ is a random Gaussian variable (mean $\langle\Delta\theta(\tau)\rangle = 0$, standard deviation $\langle\Delta\theta(\tau)^2\rangle$), its characteristic function is $\langle e^{ik\Delta\theta(\tau)}\rangle = e^{ik\langle\Delta\theta(\tau)\rangle}e^{-k^2\langle\Delta\theta(\tau)^2\rangle/2} = e^{-k^2\langle\Delta\theta(\tau)^2\rangle/2}$. Thus,

$$C_\perp(\tau) = e^{-\langle\Delta\theta(\tau)^2\rangle/2}. \tag{D7}$$

To estimate $\langle\Delta\theta(\tau)^2\rangle$, we write the one-dimensional Langevin equation associated with the rotation of the cell in the focal plane (i.e., again assuming that $H > 10$ and that the cell axis is more or less aligned with the focal plane):

$$\frac{d\theta(t)}{dt} = \frac{1}{f_{r_\perp}}\xi(t) - \frac{\mu B}{f_{r_\perp}}\sin\theta(t), \tag{D8}$$

where $\xi(t)$ is the random force associated with Brownian motion. For times smaller than the magnetic relaxation time $\tau_B = f_{r_\perp}/(\mu B)$ (in the conditions of our experiments, $\mu < 10^{-15}\,\text{A}\,\text{m}^2$, $B < 1$ mT, and $f_{r_\perp} > 10$ fN μm s, thus $\tau_B > 10$ ms), we may consider that the magnetic torque is constant, and write

$$\Delta\theta(\tau) \simeq \frac{1}{f_{r_\perp}}\int_t^{t+\tau}\xi(s)ds - \frac{\mu B}{f_{r_\perp}}\sin\theta(t)\tau. \tag{D9}$$

Then,

$$\langle\Delta\theta(\tau)^2\rangle \simeq \frac{1}{f_{r_\perp}^2}\int_t^{t+\tau}ds\int_t^{t+\tau}\langle\xi(s)\xi(u)\rangle du$$
$$+ \left(\frac{\mu B}{f_{r_\perp}}\right)^2\tau^2\langle\sin^2\theta(t)\rangle. \tag{D10}$$

As a result of the fluctuation-dissipation theorem,

$$\langle\xi(t + \tau)\xi(t)\rangle = 2df_{r_\perp}kT\delta(\tau), \tag{D11}$$

where d is the dimension of the motion ($d = 1$ here). In addition, at thermal equilibrium we have

$$\langle\sin^2\theta(t)\rangle = \int_{-\pi}^\pi \sin^2\theta e^{H\cos\theta}d\theta/[2\pi I_0(H)] = \frac{1}{H}\frac{I_1(H)}{I_0(H)}. \tag{D12}$$

Therefore,

$$\langle\Delta\theta(\tau)^2\rangle \simeq 2\frac{kT}{f_{r_\perp}}\tau + \frac{kT}{f_{r_\perp}}\frac{\mu B}{f_{r_\perp}}\frac{I_1(H)}{I_0(H)}\tau^2. \tag{D13}$$

For $\tau < \tau_B$ the second term is negligible and thus

$$C(\tau) \simeq e^{-\frac{kT}{f_{r_\perp}}\tau}. \tag{D14}$$

3. OCF in the presence of a magnetic field

To obtain an expression for the orientation correlation function (OCF) related to the apparent direction of a MTB in the focal plane in the presence of a magnetic field, we assumed that it would retain an exponential relaxation form, but no longer decay toward 0, i.e., $C_\perp(\tau) = ae^{-t/\tau_P'} + b$. The constants a, b, and τ_P' were calculated by taking into account the following constraints:
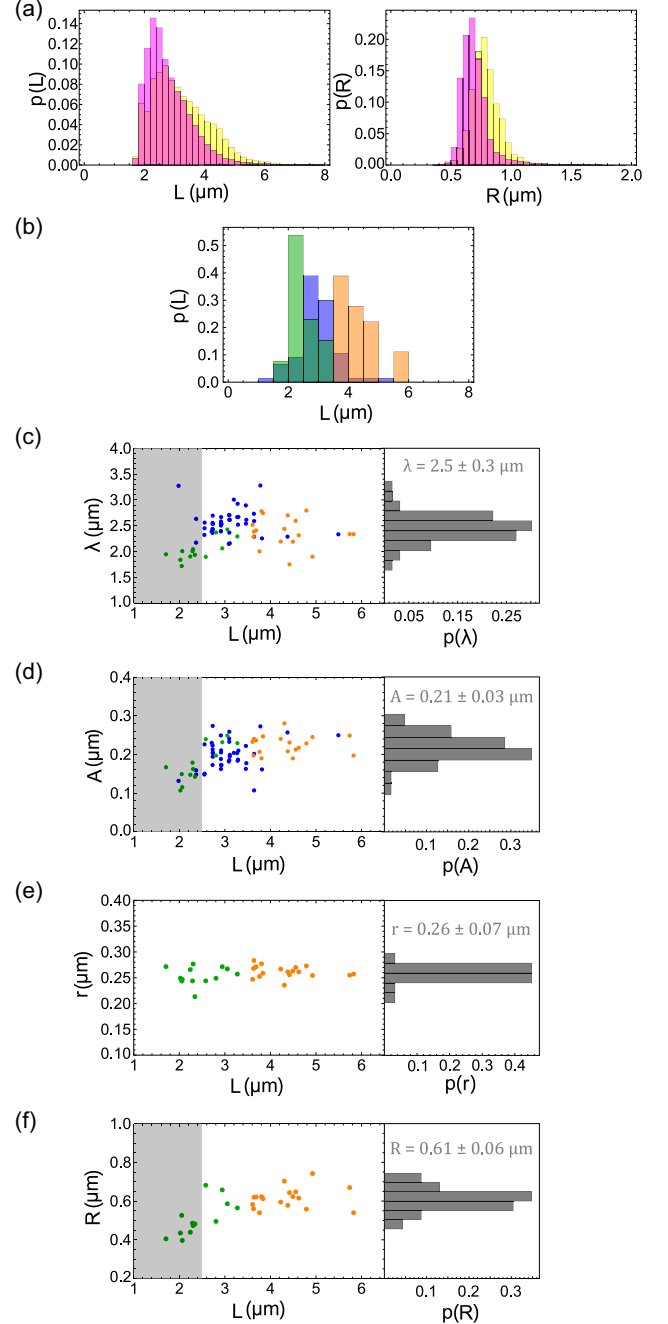

FIG. 15. Variation of cell parameters upon cephalexin treatment. (a) Distributions of cell length (L) and cell width (R) measured for AMB-1 cells in a control culture [magenta (dark gray)] and a cephalexin-treated culture [yellow (light gray)]. (b) Cell length distribution for the subset of $n = 108$ cells whose diffusion was analyzed in this work [blue (dark gray), cells grown in normal conditions and imaged at 40× magnification; green (gray), cells grown in normal conditions and imaged at 100× magnification; orange (light gray), cephalexin-treated cells imaged at 100× magnification]. [(c)–(f)] Wavelength of the cell helical backbone (c), amplitude of the cell helical backbone (d), cell body radius (e), and cell overall radius (f), as a function of cell length. Color scheme is the same as in panel (b). The distribution associated with each of these parameters is shown on the right. For panels (c), (d), and (f), the distribution only takes into account cells longer than the average wavelength $\bar{\lambda} = 2.5$ μm, for which the corresponding parameters could be measured reliably.
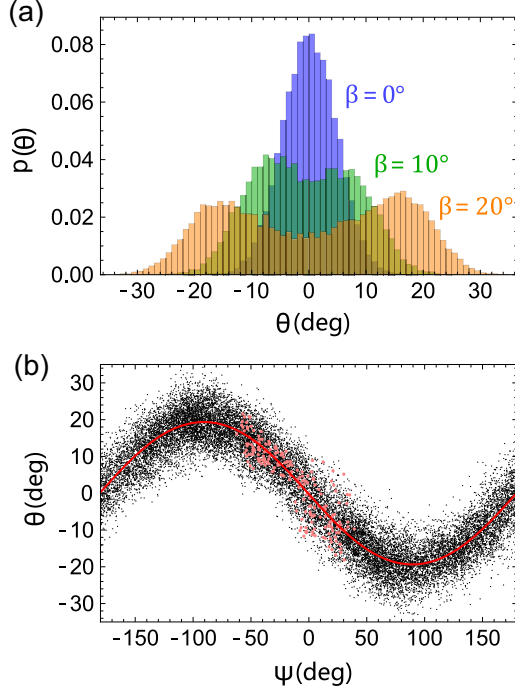
FIG. 16. Influence of a misalignment between the cell longitudinal axis $\vec{L}$ and its magnetic moment $\vec{\mu}$. (a) Orientation distributions for simulated cells placed in a magnetic field $B = 1$ mT, for simulations equivalent to a 200-s experiment. (b) Coupling between the apparent orientation in the focal plane, θ, and the apparent orientation around the cell longitudinal axis, ψ, for a misalignment angle $\beta = 20°$. The pink (gray) points show the result from the first 2 s of the simulation. The solid line is the fit to the black points (simulation equivalent to a 200-s experiment) in the form of Eq. (F1).

(i) $C_\perp(\infty) = [I_1(H)/I_0(H)]^2 = b$.

(ii) $C_\perp(0) = 1$ (neglecting any source of experimental noise), and thus $a = 1 - b$.

(iii) $\frac{dC_\perp}{d\tau}(0) = -\frac{kT}{f_{r_\perp}}$ [Eq. (D14)] and thus $\tau'_P = a f_{r_\perp}/(kT)$. Thus,

$$C_\perp(\tau) = \left(1 - \left[\frac{I_1(H)}{I_0(H)}\right]^2\right) e^{-t/\tau'_P} + \left[\frac{I_1(H)}{I_0(H)}\right]^2, \quad (D15)$$

with

$$\tau'_P = \left(1 - \left[\frac{I_1(H)}{I_0(H)}\right]^2\right) \frac{f_{r_\perp}}{kT}. \quad (D16)$$

APPENDIX E: EFFECT OF CEPHALEXIN ON CELL LENGTH AND MORPHOLOGY

As a result of addition of 10 µg/mL cephalexin to the growth medium, the length distribution of AMB-1 cells slightly shifted toward longer cells; however, other morphological parameters were mostly unaffected (Fig. 15).

APPENDIX F: EFFECT OF A MISALIGNMENT BETWEEN CELL AND MAGNETIC AXIS

We performed simulations (see Appendix B and Sec. II in the main text for details) to investigate the effect of a misalignment (β) between the cell longitudinal axis ($\vec{L}$) and its
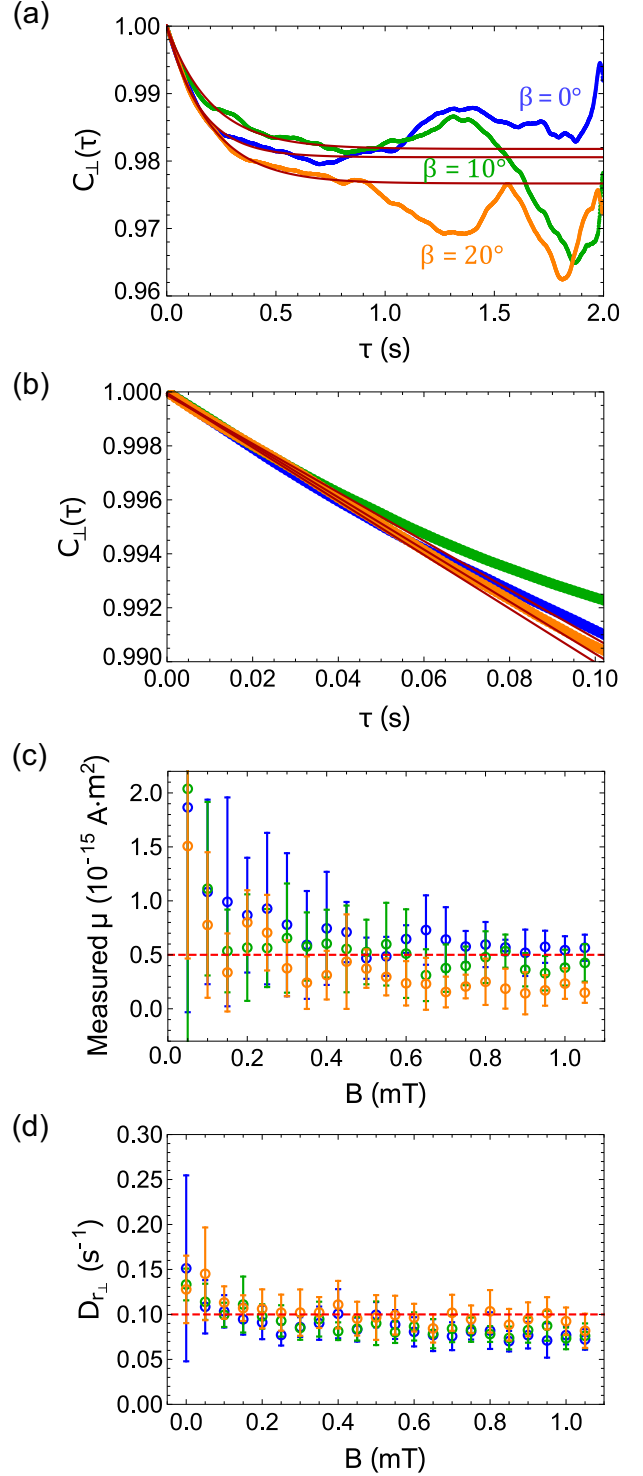

FIG. 17. (a) Influence of a misalignment on OCF for rotation perpendicular to the cell longitudinal axis, for $B = 0.5$ mT and $\beta = 0°$ [blue (very dark gray)], $\beta = 10°$ [green (dark gray)], and $\beta = 20°$ [orange (light gray)]. Lines are fit of the first 1 s of the data with Eq. (4) in the main text. (b) Closeup of the first 100 ms of the OCF shown in panel (a), with a linear fit of the first 50 ms of the data. (c) μ values obtained from fitting the OCF with Eq. (4) in the main text. (d) $D_{r_\perp}$ values obtained from fitting the first 50 ms of the OCF with a linear function. [(c), (d)] Same color scheme as in (a). [(c), (d)] The horizontal lines represent the value of μ or $D_{r_\perp}$ used in the simulations.
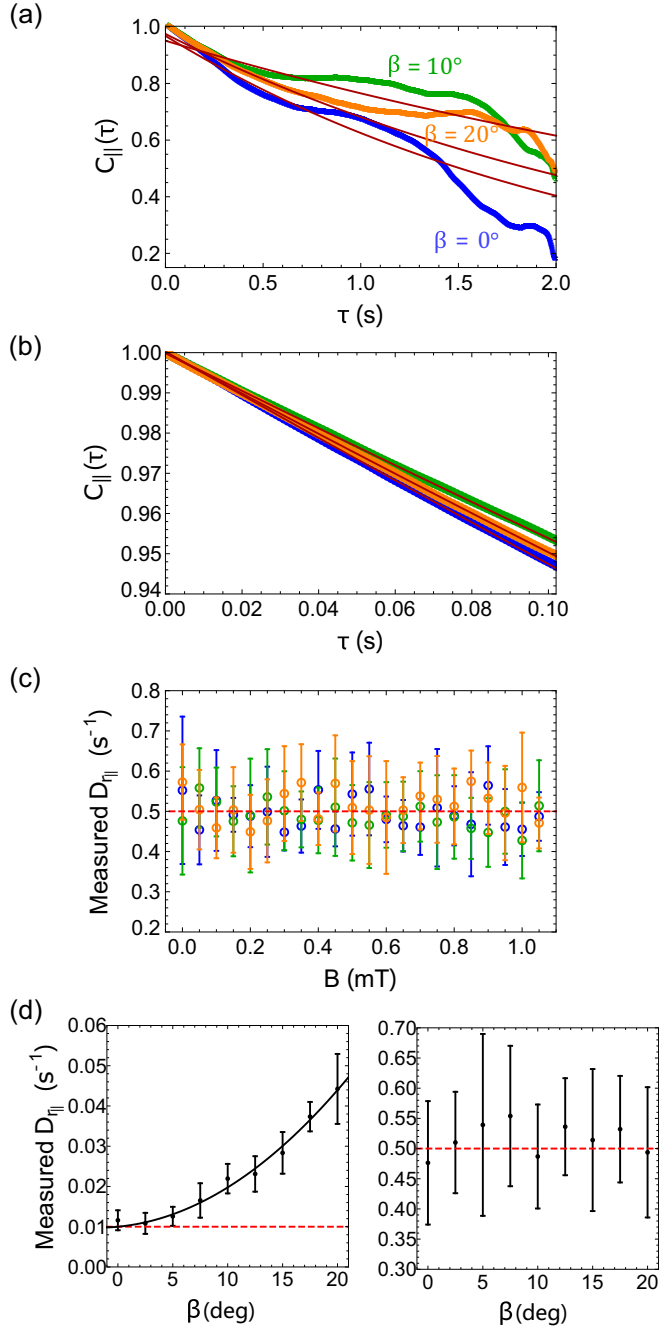
FIG. 18. (a) Influence of a misalignment on OCF for rotation parallel to the cell longitudinal axis, for $B = 0.5$ mT and $\beta = 0°$ [blue (very dark gray)], $\beta = 10°$ [green (dark gray)], or $\beta = 20°$ [orange (light gray)]. Lines are exponential fits of the first 1 s of the data. (b) Closeup of the first 100 ms of the OCF in panel (a), with an exponential fit for the first 50 ms of the data. (c) $D_{r_\parallel}$ values obtained from fitting the first 50 ms of the OCF with an exponential function as a function of B. Same color scheme as in panel (a). (d) Apparent measured $D_{r_\parallel}$ for $B = 1$ mT and either $D_{r_\parallel} = 0.01$ or 0.5 s^{-1} as a function of β. [(c), (d)] Horizontal lines represent the actual value of μ or $D_{r_\parallel}$ used in the simulation.

magnetic moment ($\vec{\mu}$) on measured OCF. This misalignment is on average $\beta = 6°$ and can be up to $\beta = 20°$ for individual *M. magneticum* AMB-1 cells [19].
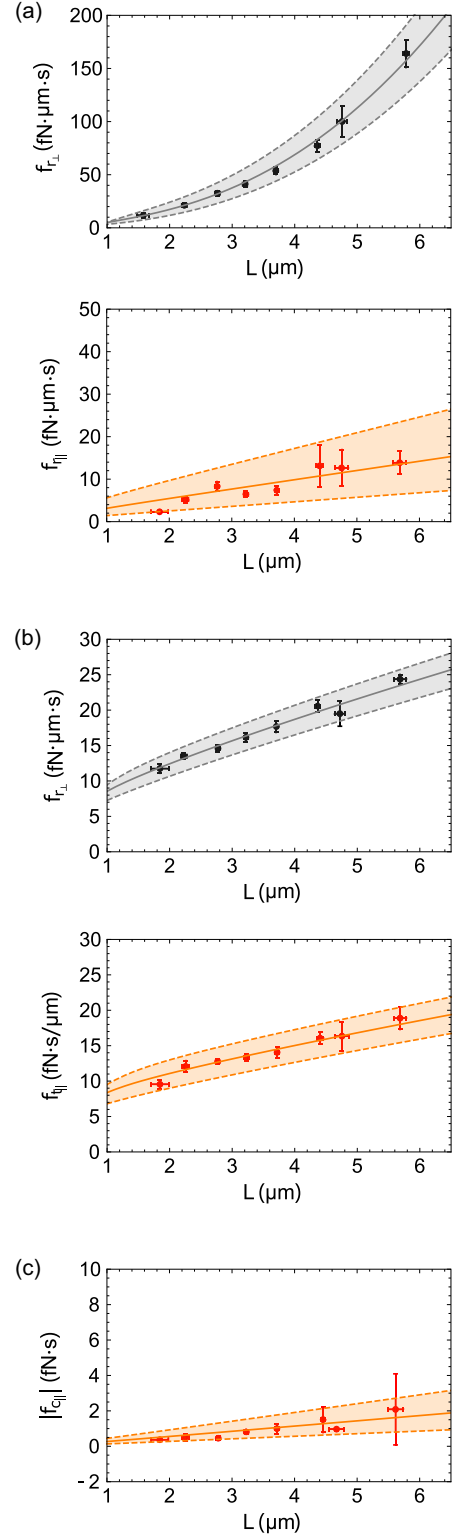

FIG. 19. Binned data for (a) rotational and (b) translational friction coefficients, and (c) longitudinal coupling friction coefficient. In panels (a) and (b), lines are fits with a cylinder model [Eqs. (A4), (A5), (A7), and (A8) in Appendix A], whereas in panel (c) the line is a fit with a helical model [Eq. (A11) in Appendix A]. The radius of the cylinder or the helix (ρ) was left to vary and found to be equal to (a) 0.51 and 0.43 μm, (b) 0.37 and 0.40 μm, and (c) 0.11 μm. Shaded areas represent the values expected for variations in the value of ρ by up to 30%.

When placed in a magnetic field ($B = 1$ mT), cells with a small or no misalignment have single-peak orientation distributions centered around $\theta = 0$; however, as β becomes larger, the distribution splits into two symmetric peaks on either side of $\beta = 0$ [Fig. 16(a)]. This change in the distribution of orientations is due to the fact that rotation of the cell around its magnetic axis ($\vec{\mu}$, which tends to be aligned with $\vec{B}$) results in a rotation of the cell longitudinal axis ($\vec{L}$). Such a rotation results in θ (rotation of the cell in the focal plane) and ψ (rotation of the cell around its longitudinal axis) being coupled in a specific way (Eq. (11) in Ref. [19]):

$$\theta(\psi) = \tan^{-1}\left(\tan\beta\cos(\psi + \delta)\right), \qquad \text{(F1)}$$

where δ is a geometrical phase shift. This relationship has been previously observed in experiments [19], and it is also clearly observed in our simulations [Fig. 16(b)]. Fitting of the experimentally observed $\theta(\psi)$ relationship with Eq. (F1) for a particular cell allows to obtain the value of β for that cell.

As can be seen in Fig. 16(b), rotational diffusion relaxation is achieved in less than 2 s (the usual length of a simulation), while capturing the relaxation of the rotation of $\vec{L}$ around $\vec{\mu}$ requires running longer experiments or simulations (here the relaxation has been achieved after 200 s). This means that the OCF associated with θ should now have two characteristic relaxation times, one associated with the diffusion of $\vec{\mu}$ around $\vec{B}$, $\tau'_P = [1 - (I_1[\mu B/(kT)]/I_0[\mu B/(kT)])^2]/D_{r_\perp}$ (see Appendix D) and one associated with the rotation of $\vec{L}$ around

$\vec{\mu}$, τ_C, where $\tau_C > \tau_P$. Calculating the OCF for only a few seconds of data, i.e., for lag times $\tau < \tau_C$, ensures that a single relaxation time is visible [Fig. 17(a)]. Fitting such OCF only for short lag time ($\tau \leqslant 1$ s) using Eq. (4) in the main text, or for even shorter lag times ($\tau \leqslant 50$ ms) with a linear fit allows to recover the value of $D_{r_\perp}$ (and, in the first case, of μ) as for cells for which $\beta = 0$ (Fig. 17).

A misalignment may also may also influence the OCF associated with $\psi(t)$, since the rotation of the cell around $\vec{\mu}$ also results in a rotation around $\vec{L}$ and therefore also affect ψ. At large $D_{r_\parallel}$ [Figs. 18(a)–18(c)], this does not affect the measurement of $D_{r_\parallel}$ obtained from the fit of the OCF for $\tau \leqslant 50$ ms. But for smaller $D_{r_\parallel}$, it can result in a quicker decay of the OCF, and an overestimated value of $D_{r_\parallel}$ [Fig. 18(d)]. It is therefore better, when trying to measure $D_{r_\parallel}$, to use only cells with a small misalignment.

APPENDIX G: BINNING AND FITTING OF THE FRICTION COEFFICIENTS

In order to verify the dependence between friction coefficient and cell lengths, the data obtained for the different friction coefficients were binned according to cell length, and fitted with the form expected for either a cylinder model ($f_{r_\perp}$, $f_{r_\parallel}$, $f_{t_\perp}$, $f_{t_\parallel}$) or a helical model ($f_{c_\parallel}$). The result of these binning and fits is shown in Fig. 19.

[1] J. Gray and G. Hancock, The propulsion of sea-urchin spermatozoa, J. Exp. Biol. **32**, 802 (1955).

[2] J. Lighthill, Flagellar hydrodynamics, SIAM Rev. **18**, 161 (1976).

[3] E. M. Purcell, Life at low Reynolds number, Am. J. Phys. **45**, 3 (1977).

[4] H. C. Berg, *Random Walks in Biology* (Princeton University Press, Princeton, NJ, 1993).

[5] H. C. Berg and R. A. Anderson, Bacteria swim by rotating their flagellar filaments, Nature (London) **245**, 380 (1973).

[6] R. M. Macnab, Bacterial flagella rotating in bundles: A study in helical geometry, Proc. Natl. Acad. Sci. USA **74**, 221 (1977).

[7] N. C. Darnton, L. Turner, S. Rojevsky, and H. C. Berg, On torque and tumbling in swimming *Escherichia coli*, J. Bacteriol. **189**, 1756 (2007).

[8] R. M. Macnab and D. Koshland, The gradient-sensing mechanism in bacterial chemotaxis, Proc. Natl. Acad. Sci. USA **69**, 2509 (1972).

[9] H. C. Berg and D. A. Brown, Chemotaxis in *Escherichia coli* analysed by three-dimensional tracking, Nature (London) **239**, 500 (1972).

[10] D. M. S. Esquivel and H. G. L. De Barros, Motion of magnetotactic microorganisms, J. Exp. Biol. **121**, 153 (1986).

[11] S. Mohammadinejad, D. Faivre, and S. Klumpp, Stokesian dynamics simulations of a magnetotactic bacterium, Eur. Phys. J. E **44**, 40 (2021).

[12] A. Bahaj, P. James, and F. Moeschler, An alternative method for the estimation of the magnetic moment of non-spherical magnetotactic bacteria, IEEE Trans. Magn. **32**, 5133 (1996).

[13] A. Chwang, T. Wu, and H. Winet, Locomotion of spirilla, Biophys. J. **12**, 1549 (1972).

[14] R. Nadkarni, S. Barkley, and C. Fradin, A comparison of methods to measure the magnetic moment of magnetotactic bacteria through analysis of their trajectories in external magnetic fields, PLoS ONE **8**, e82064 (2013).

[15] M. Reufer, R. Besseling, J. Schwarz-Linek, V. A. Martinez, A. N. Morozov, J. Arlt, D. Trubitsyn, F. Ward, and W. C. Poon, Switching of swimming modes in *Magnetospirillium gryphiswaldense*, Biophys. J. **106**, 37 (2014).

[16] C. Zahn, S. Keller, M. Toro-Nahuelpan, P. Dorscht, W. Gross, M. Laumann, S. Gekle, W. Zimmermann, D. Schüler, and H. Kress, Measurement of the magnetic moment of single *Magnetospirillum gryphiswaldense* cells by magnetic tweezers, Sci. Rep. **7**, 3558 (2017).

[17] M. Pichel, T. Hageman, I. Khalil, A. Manz, and L. Abelmann, Magnetic response of *Magnetospirillum gryphiswaldense* observed inside a microfluidic channel, J. Magn. Magn. Mater. **460**, 340 (2018).

[18] M. A. Constantino, M. Jabbarzadeh, H. C. Fu, and R. Bansil, Helical and rod-shaped bacteria swim in helical trajectories with little additional propulsion from helical shape, Sci. Adv. **2**, e1601661 (2016).

[19] L. Le Nagard, L. Yu, M. Rajkotwala, S. Barkley, D. A. Bazylinski, A. P. Hitchcock, and C. Fradin, Misalignment between the magnetic dipole moment and the cell axis in the magnetotactic bacterium *Magnetospirillum magneticum* AMB-1, Phys. Biol. **16**, 066008 (2019).

[20] https://notebookarchive.org/2022-05-5jt36c1.

[21] T. Matsunaga, T. Sakaguchi, and F. Tadakoro, Magnetite formation by a magnetic bacterium capable of growing aerobically, Applied Microbiology and Biotechnology **35**, 651 (1991).

[22] L. Le Nagard, V. Morillo-López, C. Fradin, and D. A. Bazylinski, Growing magnetotactic bacteria of the genus *Magnetospirillum*: Strains MSR-1, AMB-1, and MS-1, JoVE **140**, e58536 (2018).

[23] J. Pogliano, K. Pogliano, D. S. Weiss, R. Losick, and J. Beckwith, Inactivation of FTSI inhibits constriction of the FTSZ cytokinetic ring and delays the assembly of FTSZ rings at potential division sites, Proc. Natl. Acad. Sci. USA **94**, 559 (1997).

[24] E. Katzmann, F. D. Müller, C. Lang, M. Messerer, M. Winklhofer, J. M. Plitzko, and D. Schüler, Magnetosome chains are recruited to cellular division sites and split by asymmetric septation, Mol. Microbiol. **82**, 1316 (2011).

[25] D. Giacché, T. Ishikawa, and T. Yamaguchi, Hydrodynamic entrapment of bacteria swimming near a solid surface, Phys. Rev. E **82**, 056309 (2010).

[26] I. Wong, S. Atsumi, W.-C. Huang, T.-Y. Wu, T. Hanai, M.-L. Lam, P. Tang, J. Yang, J. C. Liao, and C.-M. Ho, An agar gel membrane-PDMS hybrid microfluidic device for long term single cell dynamic study, Lab Chip **10**, 2710 (2010).

[27] C. A. Schneider, W. S. Rasband, and K. W. Eliceiri, NIH image to ImageJ: 25 years of image analysis, Nat. Methods **9**, 671 (2012).

[28] https://notebookarchive.org/2022-05-5jsqfg2.

[29] J. Saragosti, P. Silberzan, and A. Buguin, Modeling *E. coli* tumbles by rotational diffusion. Implications for chemotaxis, PLoS ONE **7**, e35412 (2012).

[30] H. Konishi and Z. Yoshii, Determination of the spiral conformation of *Aquaspirillum* spp. by scanning electron microscopy of elongated cells induced by cephalexin treatment, Microbiology **132**, 877 (1986).

[31] D. Murat, M. Hérisse, L. Espinosa, A. Bossa, F. Alberto, and L.-F. Wu, Opposite and coordinated rotation of amphitrichous flagella governs oriented swimming and reversals in a magnetotactic spirillum, J. Bacteriol. **197**, 3275 (2015).

[32] H. Schmitzer, M. Henstridge, D. Engle, W. Dultz, and D. Tierney, Optical trapping of magnetic helical bacteria, in *Deutschen Gesellschaft für angewandte Optik (DGaO) - Proceedings* (2009), https://www.dgao-proceedings.de/download/110/110_p56.pdf.

[33] E. Lauga and T. Powers, The hydrodynamics of swimming microorganisms, Rep. Prog. Phys. **72**, 096601 (2009).

[34] See Supplemental Material at http://link.aps.org/supplemental/10.1103/PhysRevE.106.034407 for movies of bacteria swimming close to a water-glass interface.

[35] J. Saragosti, V. Calvez, N. Bournaveas, B. Perthame, A. Buguin, and P. Silberzan, Directional persistence of chemotactic bacteria in a traveling concentration wave, Proc. Natl. Acad. Sci. USA **108**, 16235 (2011).

[36] T. Kobayashi, J. Rinker, and H. Koffler, Purification and chemical properties of flagellin, Arch. Biochem. Biophys. **84**, 342 (1959).

[37] S. Tavaddod, M. A. Charsooghi, F. Abdi, H. Khalesifard, and R. Golestanian, Probing passive diffusion of flagellated

and deflagellated *Escherichia coli*, Eur. Phys. J. E **34**, 16 (2011).

[38] A. Jepson, V. A. Martinez, J. Schwarz-Linek, A. Morozov, and W. C. Poon, Enhanced diffusion of nonswimmers in a three-dimensional bath of motile bacteria, Phys. Rev. E **88**, 041002(R) (2013).

[39] G. Hancock, The self-propulsion of microscopic organisms through liquids, Proc. R. Soc. London A **217**, 96 (1953).

[40] P. B. Hylemon, J. S. Wells, Jr., N. R. Krieg, and H. W. Jannasch, The genus *Spirillum*: A taxonomic study, Int. J. Syst. Evol. Microbiol. **23**, 340 (1973).

[41] S. Chattopadhyay, R. Moldovan, C. Yeung, and X. Wu, Swimming efficiency of bacterium *Escherichia coli*, Proc. Natl. Acad. Sci. USA **103**, 13712 (2006).

[42] M. P. Hughes and H. Morgan, Measurement of bacterial flagellar thrust by negative dielectrophoresis, Biotechnol. Progress **15**, 245 (1999).

[43] C. J. Pierce, E. Osborne, E. Mumper, B. H. Lower, S. K. Lower, and R. Sooryakumar, Thrust and power output of the bacterial flagellar motor: A micromagnetic tweezers approach, Biophys. J. **117**, 1250 (2019).

[44] G. Lowe, M. Meister, and H. C. Berg, Rapid rotation of flagellar bundles in swimming bacteria, Nature (London) **325**, 637 (1987).

[45] H. C. Berg and L. Turner, Torque generated by the flagellar motor of escherichia coli, Biophys. J. **65**, 2201 (1993).

[46] X. Chen and H. C. Berg, Torque-speed relationship of the flagellar rotary motor of *Escherichia coli*, Biophys. J. **78**, 1036 (2000).

[47] M. M. Tirado and J. G. de la Torre, Translational friction coefficients of rigid, symmetric top macromolecules. Application to circular cylinders, J. Chem. Phys. **71**, 2581 (1979).

[48] J. G. de la Torre and V. A. Bloomfield, Hydrodynamic properties of complex, rigid, biological macromolecules: Theory and applications, Q. Rev. Biophys. **14**, 81 (1981).

[49] M. M. Tirado, C. L. Martínez, and J. G. de la Torre, Comparison of theories for the translational and rotational diffusion coefficients of rod-like macromolecules. application to short dna fragments, J. Chem. Phys. **81**, 2047 (1984).

[50] Y. Magariyama, S. Sugiyama, K. Muramoto, I. Kawagishi, Y. Imae, and S. Kudo, Simultaneous measurement of bacterial flagellar rotation rate and swimming speed, Biophys. J. **69**, 2154 (1995).

[51] M. M. Tirado and J. G. de la Torre, Rotational dynamics of rigid, symmetric top macromolecules. Application to circular cylinders, J. Chem. Phys. **73**, 1986 (1980).

[52] F. Perrin, Mouvement Brownien d'un ellipsoide (II). Rotation libre et dépolarisation des fluorescences. Translation et diffusion de mólecules ellipsoidales, J. Phys. Radium **7**, 1 (1936).

[53] Y. Han, A. M. Alsayed, M. Nobili, J. Zhang, T. C. Lubensky, and A. G. Yodh, Brownian motion of an ellipsoid, Science **314**, 626 (2006).

[54] B. Cichocki, M. L. Ekiel-Jeżewska, and E. Wajnryb, Brownian motion of a particle with arbitrary shape, J. Chem. Phys. **142**, 214902 (2015).

[55] H. Hoshikawa and N. Saito, Brownian motion of helical flagella, Biophys. Chem. **10**, 81 (1979).